https://doi.org/10.5194/egusphere-2026-3435
Preprint. Discussion started: 25 June 2026

Sensitivity of grounding zone melting to subglacial discharge configuration and sediment dynamics across contrasting ice shelf cavity regimes

Paola Papapetros [1,2], Benjamin K. Galton-Fenzi [3,1,2], David E. Gwyther [4,1,3], Fabio Boeira Dias [5], Sue Cook [1], and Chen Zhao [1,2]

[1]Australian Antarctic Program Partnership, Institute for Marine and Antarctic Studies, University of Tasmania, Hobart, TAS, Australia.
[2]Australian Centre for Excellence in Antarctic Science, University of Tasmania, Hobart, TAS, Australia.
[3]Australian Antarctic Division, Kingston, TAS, Australia.
[4]School of the Environment, The University of Queensland, St Lucia, QLD, Australia.
[5]University of Tasmania, Hobart, TAS, Australia.

Correspondence: Paola Papapetros (Paola.papapetros@utas.edu.au)

Abstract. Subglacial freshwater discharge plays a critical role in modulating basal melting and ocean circulation beneath ice shelves, yet the combined influence of discharge configuration, cavity thermal state, and sediment-driven morphodynamics remains poorly constrained. Using idealised ocean simulations following the ISOMIP+ framework, we investigate how subglacial discharge location, configuration (channelised versus distributed), and sediment load interact with contrasting warm and cold cavity regimes, and how these processes influence the circulation, melt, and seabed evolution at the grounding zone. Melt rates differ markedly between warm and cold regimes, with values in the warm cavity an order of magnitude higher than in the cold cavity. However, relative to no-discharge control experiments, subglacial discharge induces substantially greater local melt anomalies at the grounding line in the cold cavity, where localised melt rate increases up to ∼955 %, compared to ∼173 % in the warm regime. Discharge location and configuration further control the spatial extent of the response, with channelised inputs driving strong, localised melting, and distributed inputs producing weaker but more spatially extensive melt across the grounding zone. Sediment-laden subglacial discharge consistently reduces localised melt under channelised configurations (∼ 13% reduction in the warm regime and ∼ 16% in the cold regime), whereas its influence is negligible (<1%) when discharge is distributed. These reductions arise primarily through morphodynamic feedbacks, as sediment modifies seabed structure and circulation near the grounding zone. In the cold regime, reduced circulation promotes sediment accumulation and episodic erosion, leading to seabed and circulation changes. These results demonstrate that the impact of subglacial discharge on basal melt depends on the combined effects of cavity regime, discharge configuration, and sediment dynamics, with implications for representing grounding zone processes and basal melt parametrisations in ice-ocean models, and ultimately for ice shelves vulnerability and Antarctic Ice Sheet stability.

https://doi.org/10.5194/egusphere-2026-3435
Preprint. Discussion started: 25 June 2026

1 Introduction

The Antarctic Ice Sheet plays a central role in regulating global mean sea level, and it is the dominant source of uncertainty in future projections of sea level rise (Edwards et al., 2021; Seroussi et al., 2024; Fricker et al., 2025; Galton-Fenzi et al., 2025). A key control on ice sheet stability is the buttressing provided by floating ice shelves, which modulate the flow of grounded ice into the ocean (Pritchard et al., 2012). This buttressing is highly sensitive to basal melting, driven by ocean circulation within sub-ice shelf cavities. Despite its importance, basal melt rates remain poorly constrained, and are often represented using relatively simplified parametrisations that do not fully capture the complexity of ice-ocean interactions (Holland and Jenkins, 1999; Pelle et al., 2023; Yung et al., 2025), particularly near the grounding line, where melting exerts a stronger influence on ice dynamics (Schoof, 2007; Reese et al., 2018; Smith et al., 2020; Galton-Fenzi et al., 2025).

Basal melting is controlled by a combination of large-scale ocean forcing and local processes within the cavity, including circulation regimes that control heat transport towards the ice base (Jacobs et al., 1992; Silvano et al., 2016; Rosevear et al., 2025). These cavity regimes are often defined as "warm" and "cold", which reflect the properties of the water masses accessing the ice shelf (Jacobs et al., 1992; Holland and Jenkins, 1999; Jenkins, 2011). Warm cavity systems are characterised by the intrusion of relatively warm modified Circumpolar Deep Water (mCDW) onto the continental shelf, providing a sustained heat source that enhances ice shelf basal melting (Pritchard et al., 2012; Dutrieux et al., 2014). In contrast, in cold cavity systems, such as those influenced by High Salinity Shelf Water (HSSW), heat availability is limited and basal melting rates are generally low, with circulation often dominated by weak overturning and production of Ice Shelf Water (ISW) through melt and refreezing (Lewis, 1985; Jacobs et al., 1992). Although warm and cold cavity systems produce fundamentally different thermohaline structures, the impact of these regimes on basal melt rates is not always clear-cut, as local processes such as tides and freshwater input can modify these patterns (Silvano et al., 2016).

Tidal processes play an important role in modulating cavity exchange and increasing vertical mixing (Padman et al., 2018; Richter et al., 2022b; Xia et al., 2023; Richter et al., 2022a), introducing temporal variability in ocean stratification and melt rates (Holland, 2008; Gwyther et al., 2016). These processes are especially significant when the water column becomes shallower, as the development of a tidal front creates a well-mixed region close to the grounding line (Holland, 2008), increasing the sensitivity of localised inputs, such as subglacial freshwater discharge (Huot et al., 2021; Nakayama et al., 2021; Gwyther et al., 2023; Vaňková et al., 2025; Papapetros et al., 2025).

Subglacial water discharge provides a localized source of buoyancy that facilitates the upward heat transport toward the ice shelf base, often leading to elevated melt rates in the grounding zone (Le Brocq et al., 2013; Nakayama et al., 2021; Gwyther et al., 2023; Vaňková et al., 2025; Papapetros et al., 2025). This freshwater originates from meltwater produced at the ice sheet bed through geothermal heating and frictional processes, and is subsequently transported through subglacial hydrological channels toward the grounding line (Burton-Johnson et al., 2020; Dow et al., 2022). These subglacial networks also act as an efficient pathway for sediment transport, entraining and delivering material from the ice-bed interface into the ocean cavity (Dowdeswell et al., 2015; Overeem et al., 2017; Delaney and Adhikari, 2020; Aitken et al., 2024; Horgan et al., 2025).

https://doi.org/10.5194/egusphere-2026-3435
Preprint. Discussion started: 25 June 2026

Sediment processes within ice shelf cavities introduce an additional, often overlooked, component to ice-ocean interactions. While subglacial discharge provides a primary pathway for sediment delivery, additional inputs arise from the release of englacial debris during ice shelf basal melting ('rainout') (Smith et al., 2019) and from redistribution by ocean currents (Post et al., 2014; Wang et al., 2016; Jeromson et al., 2024). Together, these sources supply sediment that can modify both cavity water column properties and seabed morphology. Suspended sediments may influence buoyancy-driven circulation (Salcedo-Castro et al., 2013; Papapetros et al., 2025), while deposition near the grounding zone alters local bathymetry (Alley et al., 1989; Horgan et al., 2013), creating feedbacks between sediment transport, cavity circulation, and basal melt (Papapetros et al., 2025).

Over longer timescales, the geomorphic expression of sustained sediment deposition near the grounding line is the formation of grounding zone wedges (GZWs), which generate localized bathymetric highs through progressive aggradation (Anandakrishnan et al., 2007; Dowdeswell and Fugelli, 2012; Smith et al., 2019). Their development and stability are influenced by sediment properties, such as composition, grain size, and density, which, together with cavity circulation, determine how material is transported, deposited, and occasionally resuspended (Horgan et al., 2013; Salcedo-Castro et al., 2013; Sutherland et al., 2020; Wright and Thom, 2023). These short-term sedimentary processes can have lasting effects, linking immediate material redistribution to the long-term evolution and stability of grounding zone wedges (Papapetros et al., 2025). By modifying the seafloor bathymetry at the grounding zone, GZWs can affect ice dynamics and grounding line migration, creating a direct feedback with ice sheet stability (Alley et al., 1989, 2007; Anandakrishnan et al., 2007; Parizek et al., 2013; Horgan et al., 2013; Dowdeswell et al., 2015; Parizek, 2024). Importantly, their evolution reflects not only a passive response to ice flow, but also the combined effects of subglacial discharge, sediment dynamics, and the cavity background circulation (Horgan et al., 2013; Papapetros et al., 2025).

While previous studies have explored the impacts of subglacial discharge or the role of sedimentation independently, the coupled effects of subglacial freshwater fluxes, sediment transport, and evolving bathymetry on ice-ocean interactions remain poorly constrained. We address this gap by investigating how sediment-laden subglacial discharge influences ice shelf basal melting and grounding zone dynamics under contrasting cavity regimes (warm and cold) and discharge configurations (channelised and distributed). Building on our previous work (Papapetros et al., 2025), we use an ice shelf-ocean model coupled with sediments to investigate how these processes interact to modify cavity circulation, basal melt patterns, and seabed morphology, providing a unified framework to assess their combined influence on grounding zone evolution.

2 Methods

2.1 ROMS

We use the Regional Ocean Modelling System (ROMS) (Shchepetkin and McWilliams, 2005), a three-dimensional Reynolds-averaged Navier Stokes equation model, employing the Boussinesq and hydrostatic approximations. In our setup, ROMS represents vertical turbulent mixing through the K-Profile Parametrisation (KPP) scheme (Large et al., 1994). ROMS uses a terrain-following vertical coordinate framework, which allows for high resolution of the sub-ice shelf and ocean bottom

https://doi.org/10.5194/egusphere-2026-3435
Preprint. Discussion started: 25 June 2026

boundary layers. It has also been extended to account for the pressure exerted by the overlying ice shelf (Dinniman et al., 2007), and to incorporate ice-ocean thermodynamic processes that parametrize basal melting (Galton-Fenzi et al., 2012).

In ROMS, sediment transport is represented by different sediment classes, grouped into cohesive (mud) and non-cohesive (sand) particles, and is fully coupled to the hydrodynamics through feedbacks with the water column and seabed evolution (Sherwood et al., 2018). Seawater bulk density is computed as a fractional mixture of fluid mass and suspended sediment per unit volume, evolving with temperature, salinity (McDougall and Barker, 2011), and suspended sediment concentration. Each sediment class is defined by its grain size, density, settling velocity, and critical shear stress, which govern its transport, deposition, and erosion. Non-cohesive sediments are entrained when bed shear stress exceeds a size-dependent threshold, with coarser grains settling more rapidly and finer grains remaining more easily suspended, while cohesive sediments exhibit increased resistance to erosion due to inter-particle bonding and consolidation, but can remain in suspension for extended periods once resuspended. Deposition is computed in the lowermost water column layer as a function of settling velocity, particle density, volume concentration, and the baroclinic time step, whereas erosion depends on bed porosity, skin-friction shear stress, critical shear stress, sediment grain density, and sediment availability in the uppermost bed layer, with erosion occurring only when the applied shear stress exceeds the critical threshold (Sherwood et al., 2018).

2.2 Model Setup and Experiments Design

We used the Ice Shelf-Ocean Model Intercomparison Project (ISOMIP+; Asay-Davis et al. (2016)) cavity domain, whose geometry (480 km along and 80 km across the ice shelf, with a maximum depth of 618 m) is comparable to that of the Pine Island Glacier Ice Shelf. The horizontal resolution is 2 km, and the vertical grid is represented by twenty-one vertical layers, with a resolution of 0.4 m at the bottom and surface layers and thickening towards the middle of the water column.

Initial conditions of ocean tracers follow Ocean1 and Ocean2 configurations, for WARM and COLD profiles, respectively (ISOMIP+; Asay-Davis et al. (2016)). Ocean1 (WARM) is characterised by a relatively cold initial water column with a warm forcing in the open boundary, with temperatures vertically ranging from - 1.9 to 1°C, and salinity from 33.8 to 34.7. Ocean2 (COLD) features a warmer initial state with colder boundary forcing, with salinity vertically ranging from 33.8 to 34.55, and a linear temperature profile of - 1.9°C (see Asay-Davis et al. (2016) for full details). In both regimes, the concentration of suspended sediment in the water column is initialised as zero. Tidal forcing is then prescribed using a single component (semidiurnal $M2$ harmonic constant with 12 hours frequency) and a cosine function with an amplitude of 0.1 m/s (following (Gwyther et al., 2016)). The tidal forcing is initiated with a hyperbolic tangent ramp to prevent numerical instabilities, which gradually increases the tidal signal from zero at the beginning of the simulation with a 1-day ramping timescale.

The subglacial drainage is prescribed with zero salinity and a potential temperature of $\sim$ - 0.007°C, equal to the freezing point at the mean pressure (McDougall and Barker, 2011) between the ice shelf base and the bathymetry at the grounding line. The subglacial water discharge is applied as a momentum flux, uniformly distributed across all vertical layers of the water column (following Gwyther et al. (2023) and Papapetros et al. (2025)) and held constant at 72 $m^3 s^{-1}$ (based on Vaňková et al. (2025), for future melt rates comparison), and acts as a source of sediment discharge.

https://doi.org/10.5194/egusphere-2026-3435
Preprint. Discussion started: 25 June 2026

The prescribed subglacial flux is relatively high (e.g. compared to Nakayama et al. (2021), Gwyther et al. (2023) and Papapetros et al. (2025)), so we prescribed a relatively high sediment concentration of 1 kg m^{-3} (compared to $\sim$ 0.08 kg m^{-3} for low-flux conditions) and a grain density of 2650 kg m^{-3} (following Aitken et al. (2024)). Equal proportions of two cohesive (mud) and two non-cohesive (sand) sediment classes are prescribed (0.004, 0.04, 0.5, and 1 mm for Mud1, Mud2, Sand1, and Sand2, respectively) and applied to both the initial bed composition and the subglacial suspended input, ensuring consistency between bed and input sediment composition (Papapetros et al., 2025). The seabed sediment layer is initialised with a thickness of 1 m. A new depositional layer is formed once accumulation exceeds 0.01 m, which controls the model's sensitivity to sediment storage and stratigraphic evolution by regulating how frequently new layers are created and how depositional variability is recorded (Sherwood et al., 2018). Consistent with the ROMS framework, sediment particles are assumed to be in thermodynamic equilibrium with the surrounding water, as their temperature and salinity are not explicitly represented here.

A total of 62 experiments were conducted to investigate cavity dynamics under both warm and cold regimes. All simulations reached a quasi-steady state over 20 years (Figure A1, Appendix A), and our analyses were based on the averaged fields from the last 6 months of simulation to account for free surface variability. For each regime, we established baseline experiments (*Control*$_0$*_warm* and *Control*$_0$*_cold*), which incorporate tidal forcing and sediment re-mobilisation in the uppermost sediment layer at the bottom of the cavity, but no input from the subglacial system.

Our experiments were divided into four main sections. Section 3.1 focusses on assessing the general influence of sediment-laden subglacial discharge on cavity dynamics, in which we conducted experiments with a single subglacial channel centrally located at 38 km (*Sgw+Sed*$_{38}$*_warm* and *Sgw+Sed*$_{38}$*_cold*). In Section 3.2, we expand the investigation to explore the role of the discharge location under both regimes (*Sgw+Sed*$_x$*_warm* and *Sgw+Sed*$_x$*_cold*). The subscript index $_x$ refers to the 14 different locations of the subglacial discharge, ranging from 20 km to 58 km along the grounding line (Figure 1). To assess the relative contributions of freshwater-only and sediment-laden discharge to basal melt variability, an additional set of simulations without sediment input was further conducted (Sgw$_x$_warm and Sgw$_x$_cold). In Section 3.3, we investigate the impact of distributed discharge, by applying the same total flux, uniformly divided across the 14 locations, distributing both the fresh outflow (*Sgw*$_D$*_warm* and *Sgw*$_D$*_cold*) and sediment (*Sgw+Sed*$_D$*_warm* and *Sgw+Sed*$_D$*_cold*). Finally, in Section 3.4, we compare the effects of distributed versus channelised discharge on melt rates across both cavity regimes. The analysis was conducted at two spatial scales: locally at the grounding line, defined as the first grid cell adjacent to each discharge location, and regionally using area-averaged values across the grounding zone. In this study, we define the grounding zone as the region extending up to 8 km downstream of the grounding line, where the influence of the subglacial outflow has the greatest impact in the cavity dynamics (Figure 1).

3 Results

3.1 General Cavity Dynamics

Our control experiments (*Control*$_0$*_warm* and *Control*$_0$*_cold*) reveal contrasting cavity states prior to the introduction of subglacial discharge (Figure 2). In both regimes, the barotropic circulation is characterized by a broad clockwise (positive) circu-

https://doi.org/10.5194/egusphere-2026-3435
Preprint. Discussion started: 25 June 2026

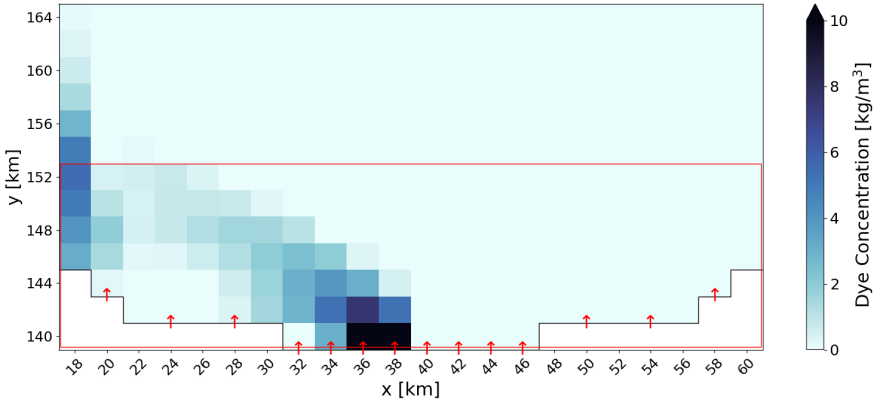

Figure 1. Illustration of the area close to the grounding line in the ISOMIP+ cavity, with the fresh discharge location at x = 38 km. Dye concentration summed throughout the water column is used to delineate the cavity circulation. The x axis represents the cross-shelf direction (west to east), and the y axis represents the along-shelf direction (south to north). The red rectangle delineates the grounding zone, defined here based on the area where the subglacial outflow has the greatest impact. Red arrows indicate all locations where subglacial discharge was applied, for either channelised or distributed outflow experiments. The cavity geometry remains unchanged for both warm and cold regimes.

lation cell occupying much of the grounding zone region, and a weaker anticlockwise (negative) circulation near the eastern boundary (Figure 2a; Yung et al. (2026)). This circulation structure promotes the transport of relatively warmer and saltier waters toward the eastern grounding zone, contributing to the asymmetric distribution of temperature, salinity, and melt rate observed in both control states (Figure 2b-d). Despite these common features, the cavity regimes differ substantially in circulation strength and spatial organization. The warm control (*Control*$_0$*_warm*) exhibits a stronger cavity circulation overall, with a spatially diffuse anticlockwise circulation cell near the eastern boundary, and an additional weaker anticlockwise circulation feature along the western cavity margin (Figure 2a). In contrast, the cold control (*Control*$_0$*_cold*) exhibits a simpler circulation pattern along the western boundary, characterized by the absence of two circulation cells and the dominance of a single clockwise circulation cell (Figure 2a). The barotropic streamfunction ranges approximately from -10 to 19 mSv, with maximum positive values reaching 18.7 mSv in the *Control*$_0$*_warm* and 9.3 mSv in the *Control*$_0$*_cold* (Figure 2a).

In the experiments including subglacial water discharge ([*Sgw*+*Sed*$_{38}$*_warm*] and [*Sgw*+*Sed*$_{38}$*_cold*]), the strong salinity contrast between the freshwater outflow (salinity = 0) and ambient cavity waters (33.61 to 34.65) generates an energetic buoyant current near the discharge location that reorganizes the pre-existing cavity circulation (Figure 2a,b). In both regimes, the buoyant outflow simultaneously intensifies the western clockwise circulation cell and the eastern anticlockwise circulation cell. As the eastern cell expands westward into the region previously occupied by the western circulation cell, the boundary between the two cells becomes increasingly important in controlling the thermohaline dynamics at the grounding zone (Figure 2a-d).

Salinity fields primarily reflect cavity circulation, with a further freshwater signature in the discharge experiments due to the buoyant outflow. In *Control*$_0$*_warm* and *Control*$_0$*_cold* cases, upper-layer salinity is higher where ambient water is recirculated

https://doi.org/10.5194/egusphere-2026-3435
Preprint. Discussion started: 25 June 2026

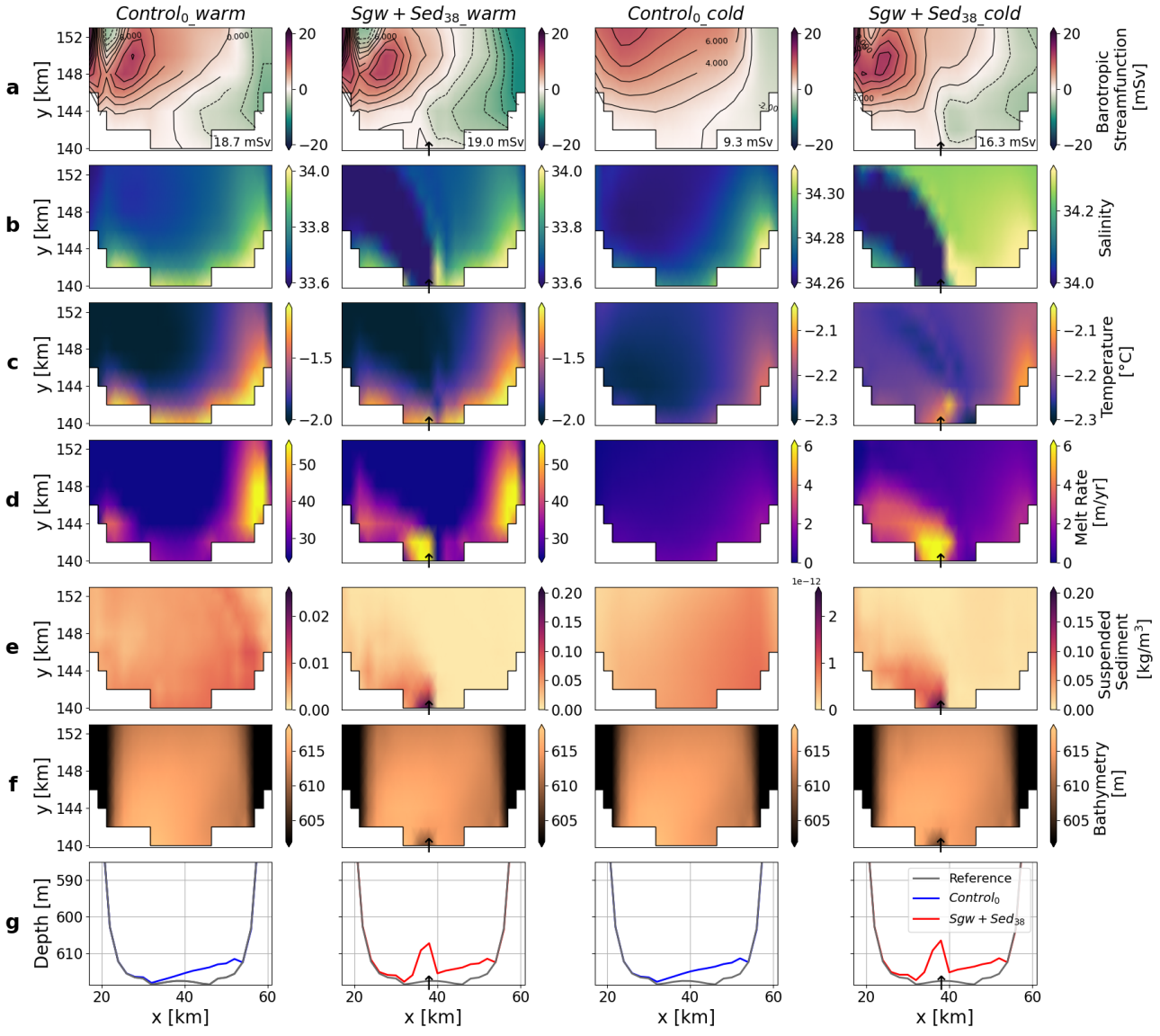

Figure 2. Grounding zone absolute values from the simulations *Control*$_0$*_warm*, *Control*$_0$*_cold*, *Sgw+Sed*$_{38}$*_warm* and *Sgw+Sed*$_{38}$*_cold*. The latter experiments include channelised sediment-laden subglacial discharge at the location x=38 km. Panels show barotropic streamfunction (a), salinity (b) and temperature (c) at the uppermost ocean layer, melt rates (d), total concentration of suspended sediment in the water column (e), bathymetry (f) and a vertical cross-section of the grounding line geometry (g). In panel (a), the maximum positive barotropic streamfunction value for each experiment is indicated on the corresponding panel. In panel (g), the grounding line, which is non-linear in plan view, is projected onto a straightened along-grounding line coordinate, with values interpolated onto a common axis for visualization purposes. Note the differing colour scales used for salinity, temperature, melt rate and suspended sediment fields.

https://doi.org/10.5194/egusphere-2026-3435
Preprint. Discussion started: 25 June 2026

toward the grounding line (Figure 2a,b). In contrast, the subglacial outflow (*Sgw+Sed*$_{38}$*_warm* and *Sgw+Sed*$_{38}$*_cold*) generates a low-salinity signal extending westward from the discharge outlet, alongside a higher-salinity anticlockwise circulation cell in the east (Figure 2a,b). In both regimes, the strong freshwater signal suggests that the buoyant outflow is transported along the reorganized circulation pathways, extending preferentially downstream within the clockwise circulation cell (Figure 2a,b). Moreover, the cold regime exhibits a broader and stronger spatial impact on salinity fields relative to the warm regime, consistent with reduced meltwater production and weaker background circulation within the grounding zone (Figure 2a,b).

The buoyant outflow further modifies the temperature structure and basal melt distribution at the grounding zone (Figure 2c,d). In the warm regime, the interaction between the two opposing circulation cells enhances the thermal contrast at the grounding zone, with the western clockwise circulation exporting relatively warmer waters ($\sim$ - 1.16°C) away from the discharge site, while the eastern anticlockwise circulation recirculates comparatively colder waters ($\sim$ - 1.54°C) towards the grounding line (Figure 2a,c). Melt rate patterns exhibit a similar spatial structure with higher rates on the western side of the discharge site ($\sim$ 78.5 m yr^{-1}) and lower melt rates on the eastern side ($\sim$ 18.5 m yr^{-1}; Figure 2d), indicating that basal melting directly reflects the circulation-driven redistribution of ocean heat. On the other hand, despite the stronger circulation reorganization induced by the buoyant outflow, the cold regime remains comparatively colder ($\sim$ - 2.3 to - 2°C) and more spatially uniform, limiting the thermal response and maintaining lower absolute melt rates (9.8 and 2.3 m yr^{-1} on the western and eastern sides of the discharge site, respectively) relative to the warm regime (Figures 2a,c,d).

The background circulation also controls sediment transport and deposition patterns at the grounding zone. In the warm regime, the stronger cavity circulation promotes greater sediment remobilisation and downstream transport, maintaining comparatively more sediment in suspension and limiting local accumulation near the discharge site (Figure 2e-g). In contrast, the weaker circulation in the cold regime enhances sediment retention within the grounding zone, favouring comparatively slightly greater local deposition (Figure 2f,g and Figure A2, Appendix A). Although suspended sediment concentrations remain low in both scenarios ($<$ 0.02 kg m^{-3} in the warm regime, and very close to zero in the cold regime), differences in circulation strength produce distinct bathymetric elevations (Figure A2, Appendix A). In both regimes, sediment-laden subglacial discharge generates measurable seabed modification adjacent to the discharge location, with bathymetric increases of up to 9-10 m (Figure 2f,g and Figure A2, Appendix A). However, the cold cavity also exhibits slightly greater deposition of subglacial sediments and hence growth of bathymetry near the grounding line, relative to the warm regime, consistent with enhanced sediment retention at the grounding zone and reduced downstream export.

Together, these results demonstrate that subglacial buoyancy forcing fundamentally reorganizes cavity circulation, which in turn governs the redistribution of heat, melt, and sediment deposition, ultimately modulating the dynamics and the localized bathymetric evolution at the grounding zone.

3.2 Impact of Channelised Subglacial Discharge Location

In this section, we examine how the location of sediment-laden subglacial discharge along the grounding line influences cavity dynamics under both warm and cold regimes (*Sgw+Sed*$_x$*_warm* and *Sgw+Sed*$_x$*_cold*). Figures 3 and 4 illustrate the grounding zone response across circulation, thermohaline structure, melt rates, suspended sediment concentration, and bathymetric

https://doi.org/10.5194/egusphere-2026-3435
Preprint. Discussion started: 25 June 2026

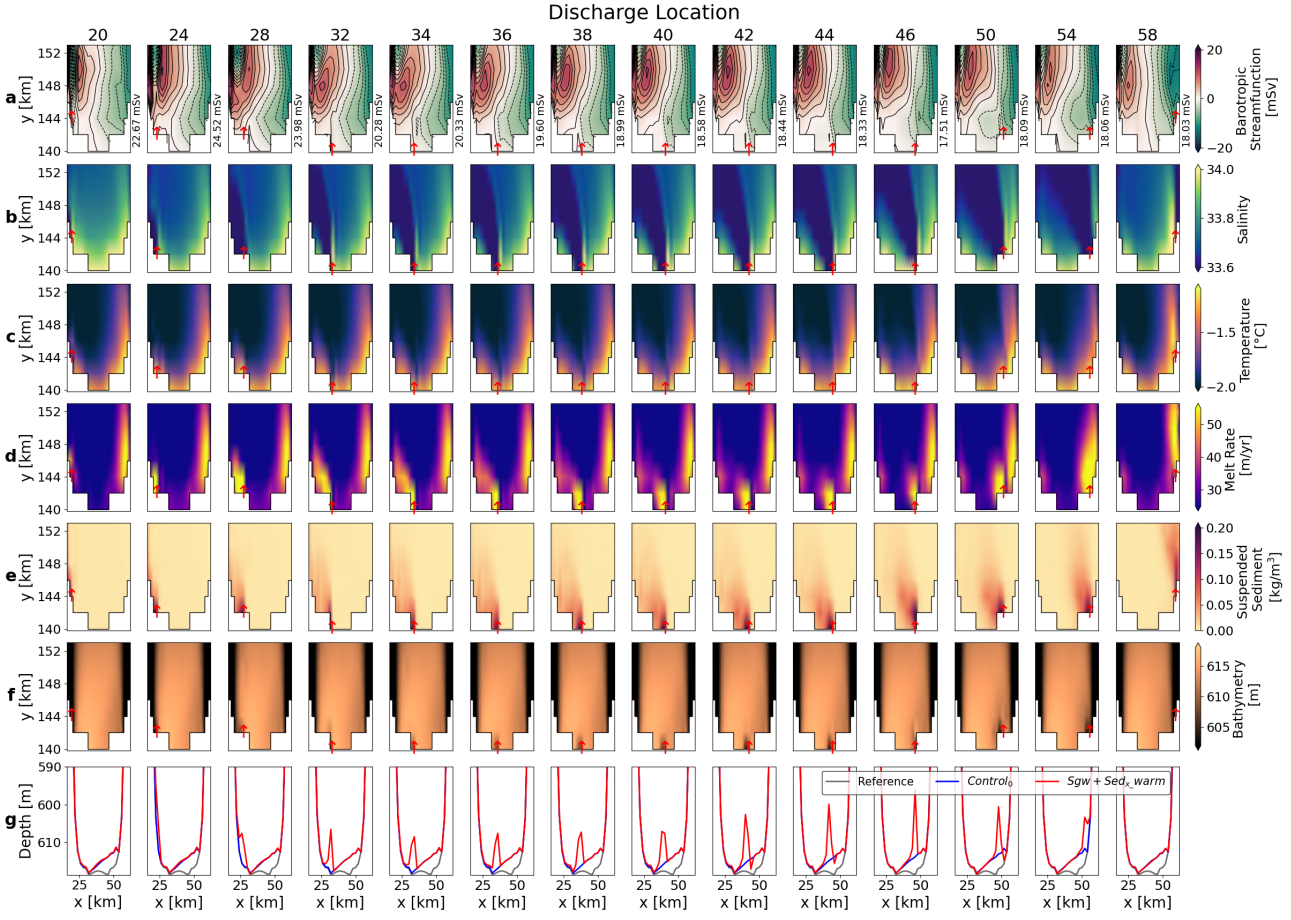

Figure 3. Warm regime absolute values from the simulations with different subglacial freshwater and sediment discharge locations ([*Sgw+Sed*$_x$*_warm*). Injection sites range from 20 to 58 and are indicated by red arrows. Each column represents a distinct grounding line injection site (*Sgw+Sed*$_x$*_warm*), progressing from west (left) to east (right), while each row shows barotropic streamfunction (a), salinity (b) and temperature (c) at the uppermost ocean layer, melt rates (d), total concentration of suspended sediment in the water column (e), bathymetry (f) and a vertical cross-section of the grounding line geometry (g). In panel (a), the maximum positive barotropic streamfunction value for each experiment is indicated on the right side of the corresponding panel. In panel (g), the grounding line, which is non-linear in plan view, is projected onto a straightened along-grounding line coordinate, with values interpolated onto a common axis for visualization purposes.

evolution. Across both cavity regimes, discharge location exerts a first-order control on grounding zone dynamics and buoyant outflow evolution. In general, western and easternmost discharge sites remain strongly influenced by adjacent boundaries, pro-
205 ducing spatially confined responses, whereas central and central-eastern discharge locations interact more efficiently with the cavity interior and generate broader grounding zone-scale differences.

https://doi.org/10.5194/egusphere-2026-3435
Preprint. Discussion started: 25 June 2026

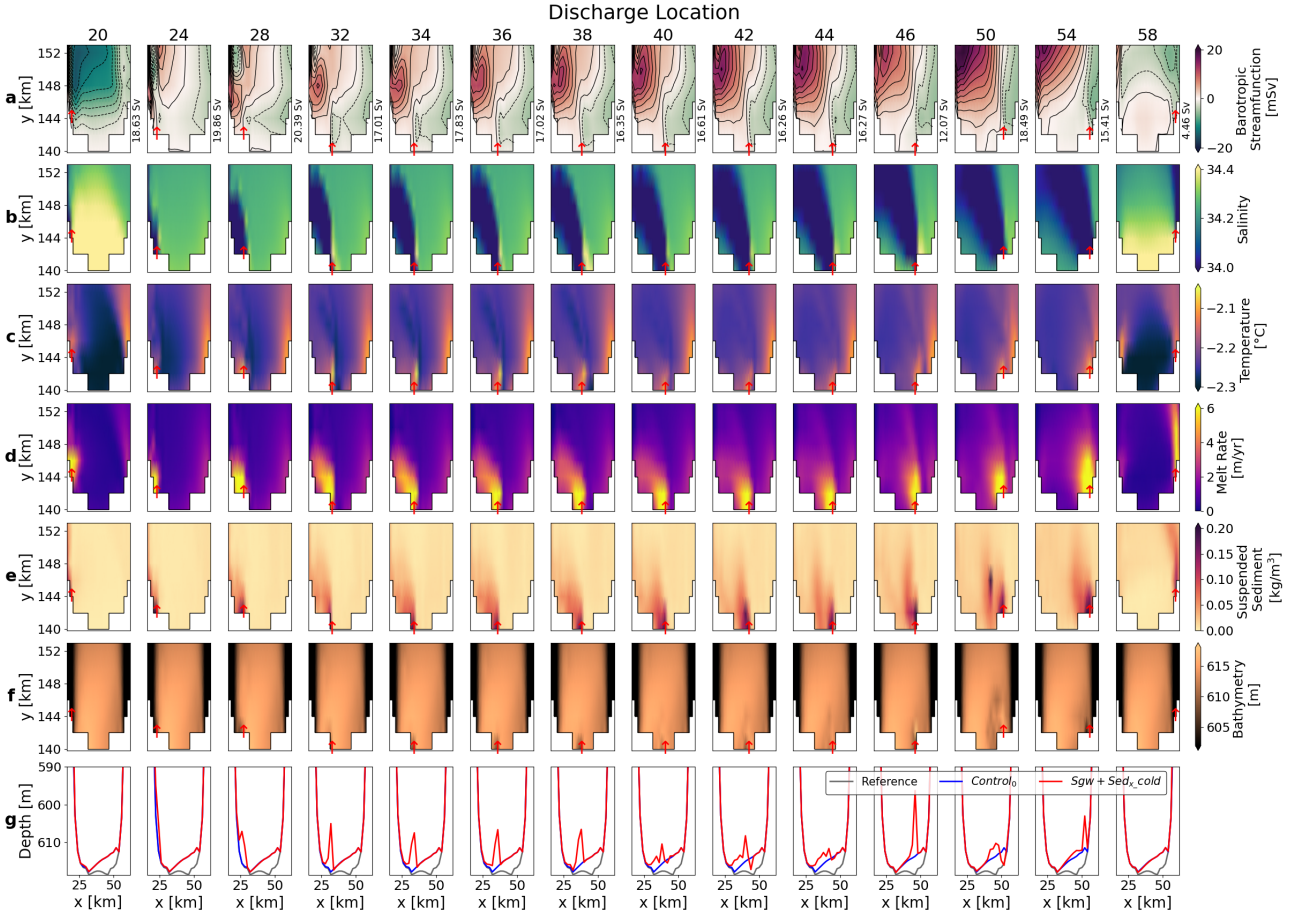

Figure 4. Cold regime absolute values from the simulations with different subglacial freshwater and sediment discharge locations ([*Sgw+Sed*$_x$*_cold*). Injection sites range from 20 to 58 and are indicated by red arrows. Each column represents a distinct grounding line injection site (*Sgw+Sed*$_x$*_cold*), progressing from west (left) to east (right), while each row shows barotropic streamfunction (a), salinity (b) and temperature (v) at the uppermost ocean layer, melt rates (d), total concentration of suspended sediment in the water column (e), bathymetry (f) and a vertical cross-section of the grounding line geometry (g). In panel (a), the maximum positive barotropic streamfunction value for each experiment is indicated on the right side of the corresponding panel. In panel (g), the grounding line, which is non-linear in plan view, is projected onto a straightened along-grounding line coordinate, with values interpolated onto a common axis for visualization purposes.

The spatial structure of the buoyant outflow and associated circulation response strongly depends on the discharge location (Figures 3a,b and 4a,b). Central and central-eastern discharge locations align more with the boundary between the opposing circulation cells, allowing the buoyant forcing to directly influence both cells simultaneously (discharge locations 28 to 50; Figures 3a,b and 4a,b). In these configurations, the clockwise circulation preferentially transports fresher discharge waters away from the grounding line and towards the cavity interior, while the anticlockwise circulation recirculates comparatively

https://doi.org/10.5194/egusphere-2026-3435
Preprint. Discussion started: 25 June 2026

warmer and saltier waters back towards the grounding zone (Figures 3a-c and 4a-c). Consequently, central and central-eastern discharges generate broader thermohaline redistribution and stronger grounding zone-scale circulation reorganization. In contrast, the fresh outflow in western (20 and 24) and eastern (54 and 58) discharge locations remains more strongly constrained by the adjacent cavity boundaries. Under these configurations, the buoyant outflow interacts primarily with a single circulation cell, limiting downstream freshwater export and promoting localized freshwater retention near the discharge site (Figures 3a,b and 4a,b). This geometric confinement is substantially stronger in the warm regime, where the energetic background circulation prevents the buoyancy forcing from reorganizing the wider grounding zone circulation (discharge locations 20, 24, 50 and 58; Figure 3a). In the cold regime, however, the weaker ambient circulation allows even boundary-confined discharges to influence a much larger fraction of the grounding zone circulation structure (Figure 4a).

These circulation adjustments subsequently control the redistribution of ocean heat and the resulting melt rate response (Figures 3c,d and 4c,d). In the warm regime, central and central-eastern discharges enhance the thermal contrast at the grounding line by strengthening the separation between the freshwater export pathway associated with the clockwise circulation and the recirculation of warmer waters toward the grounding line by the anticlockwise circulation (discharge locations 24 to 54; Figures 3a,c). This generates the distinct spatial temperature structure observed across the grounding zone, which is mirrored by melt rate patterns (Figure 3c,d). Localized cooling in the upper-layer persists east of several discharge sites driven by the recirculation of colder cavity water within the anticlockwise circulation cell (Figure 3a,c,d). In contrast, the cold regime exhibits a comparatively more spatially uniform temperature and melt rate structure despite the stronger circulation reorganization (Figures 4a,c,d). This reflects the smaller thermal contrast between the ambient cavity waters and the subglacial outflow, which limits the development of strong thermal gradients even when circulation adjustments are substantial (Figures 4a,c). A more detailed quantitative analysis of melt rates is presented in Section 3.4.

Suspended sediment transport and bathymetric evolution similarly respond to the circulation structure established by the buoyant outflow (Figures 3e-g and 4e-g). In both cavity regimes, the highest concentrations of suspended sediment occur near the discharge locations, where buoyant outflow entrains and redistributes sediment along the circulation pathways (Figures 3e and 4e). The stronger background circulation in the warm regime enhances downstream sediment export, maintaining comparatively lower suspended sediment concentrations at the grounding zone and limiting local deposition (Figures 3e-g and A2, Appendix A). Conversely, the weaker circulation and reduced flushing efficiency of the cold regime favour sediment retention near the grounding line, sustaining broader suspended sediment persistence and promoting more pronounced depositional features near the discharge location (Figures 4e-g and A2, Appendix A).

The depositional environments formed in the cold regime are additionally characterised by episodic erosion events that are largely absent in the warm simulations (Figures 3g and 4g, and A3, Appendix A). These events occur primarily at central-eastern discharge locations (40, 42, 44 and 50), where the anticlockwise circulation tends to be confined between the evolving bathymetry and the grounding line eastern boundary geometry (Figure 4a,f,g). Rapid reductions in local bathymetric height coincide with sharp increases in suspended sediment concentration and substantial rearrangement of the grounding zone seabed (Figure 4e-g). Using the central experiment *Sgw+Sed*$_{40}$*_cold* as an illustrative case, we show that these erosion events arise from the interplay between grounding zone geometry, weak background circulation, depositional environment and bed sedi-

https://doi.org/10.5194/egusphere-2026-3435
Preprint. Discussion started: 25 June 2026

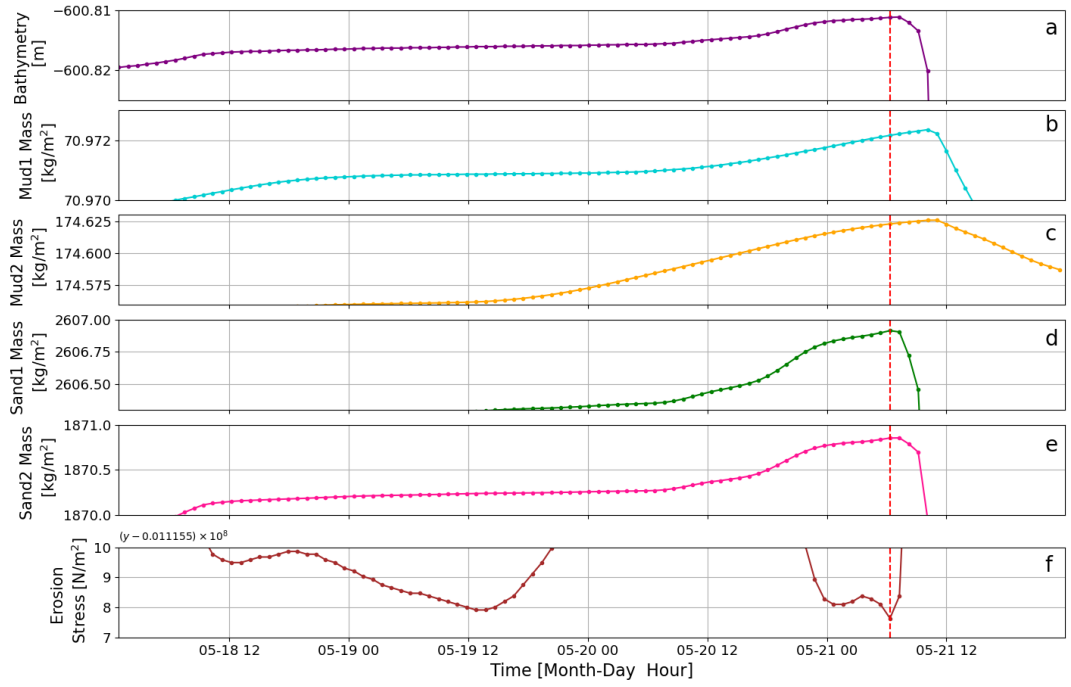

Figure 5. Time series of geophysical evolution during an erosion event on the illustrative central experiment *Sgw+Sed*$_{40}$*_cold*. Panels show (a) bathymetric elevation, mass of (b) Mud1, (c) Mud2, (d) Sand1, and (e) Sand2 in the uppermost seabed layer, and (f) bed erosion stress. The red dashed line marks the threshold of the event, which is accompanied by an abrupt increase in shear stress and subsequent loss of sediment mass. Note the different y axis offset in panel (f) due to the small value range, which spans 0.01115507 to 0.0111551 N/m^2.

ment composition (Figures 4a,f,g and 5a-e). Reduced cavity velocities favour enhanced sediment accumulation and the formation of sand-rich depositional beds (Figure 5c-f), reflecting the preferential settling of coarse particles with higher settling velocities relative to mud fractions (Figure A3, Appendix A). These deposits are additionally associated with comparatively low critical erosion stresses (Figure 5f), making them highly susceptible to remobilisation during moderate flow perturbations. Consequently, despite enhanced deposition, the cold regime also experiences frequent erosional reworking that partially offsets net bathymetric growth by destabilising the seabed and releasing large volumes of sediment back into suspension (Figures 4e-g and A3, Appendix A). Together, these results demonstrate that grounding line discharge location fundamentally controls how buoyant subglacial outflows interact with cavity circulation and geometry, thereby governing the redistribution of heat, melt, and sediment beneath the ice shelf and modulating the stability of grounding zone depositional environments.

3.3 Distributed Subglacial Discharge Impact

In this section, we investigate the impact of distributed subglacial discharge on grounding zone dynamics under both warm and cold regimes (*Sgw*$_D$*_warm* and *Sgw*$_D$*_cold*). Figure 6 illustrates the cavity response across circulation and thermohaline structure, melt rates, suspended sediment concentration, and bathymetric evolution. In contrast to the channelised experiments,

https://doi.org/10.5194/egusphere-2026-3435
Preprint. Discussion started: 25 June 2026

distributed discharge introduces freshwater continuously along the grounding line, generating a spatially distributed buoyancy forcing that suppresses the formation of localized buoyant jets and promotes broader grounding zone adjustment.

The distributed freshwater input reorganizes the grounding zone circulation in both cavity regimes, when compared to the control scenarios (Figures 2a,b and 6a,b). Rather than generating localized recirculation centred on a single discharge site, the distributed forcing strengthens and laterally expands the anticlockwise circulation across much of the grounding zone (Figure 6a). This circulation restructuring is more pronounced in the cold regime, where the weaker background circulation produces a proportionally larger impact from buoyancy forcing (Figure 6a). Consequently, fresh signals become more spatially distributed along the grounding zone, instead of producing jet-like freshwater structures such as in the channelised discharge experiments (Figures 3b, 4b and 6b).

These circulation changes subsequently modify temperature and melt-rate structures at the grounding zone, in comparison with the control cases (Figures 2c,d and 6c,d). In both regimes, distributed discharge preserves the spatial temperature structure of the respective control experiment, but alters the magnitude of the distribution of heat near the grounding line. In the warm regime, the distributed buoyancy forcing enhances the colder water intrusion across the central grounding zone, producing slightly lower temperatures and reduced melt rates relative to the control (Figures 2c,d and 6c,d). In contrast, the cold regime exhibits a broader warming response and enhanced melt rates across much of the grounding zone, consistent with the grounding zone-wide circulation reorganization induced by the distributed freshwater input (Figures 2a,c,d and 6a,c,d). Compared to the channelised experiments, these responses are spatially smoother and less localized, reflecting the absence of focused jet-like buoyant outflows (Figures 3b, 4b and 6b). A more detailed quantitative analysis of melt rates is presented in Section 3.4.

The distributed discharge also releases sediment through multiple low-intensity sources, preventing the formation of buoyant jet-like outflows at the grounding zone (Figure 6e). The faster circulation in the warm regime limits local sediment retention, resulting in uniformly low concentrations ($\sim 1 \times 10^{-3}$ kg m^{-3}) due to relatively efficient downstream transport (Figure 6e). In contrast, the weaker circulation in the cold cavity results in suspended sediment retention and local convergence within the grounding zone, allowing concentrations to build up to $\sim 1 \times 10^{-2}$ kg m^{-3}, producing distinct suspended sediment patterns (Figure 6e).

Finally, the suspended sediment retention in the cold regime results in more pronounced depth and bathymetry profiles (Figure 6f,g), with averaged increases in grounding line bathymetry relative to the warm cavity (Figure A2, Appendix A), similar to the channelised discharge scenarios (Figure 4f,g and A2, Appendix A). While both regimes exhibit deposition of up to 2 m adjacent to the grounding line (relative to their respective controls: *Control*$_0$*_warm* or *Control*$_0$*_cold*), the cold cavity also exhibits more extensive sediment remobilisation along the grounding zone (Figure 6f,g). Together, these results demonstrate that distributed subglacial discharge modifies grounding zone dynamics primarily through cavity-wide buoyancy forcing, which reorganizes circulation and subsequently governs the redistribution of heat, melt, and sediment.

3.4 Differences Between Channelised and Distributed Discharge on Melt Rates

In this section, we investigate the impact of distributed versus channelised flow on ice shelf basal melt rates for both cavity regimes (Figure 7). Melt responses were evaluated using local estimates at the grounding line, and regionally using averages

https://doi.org/10.5194/egusphere-2026-3435
Preprint. Discussion started: 25 June 2026

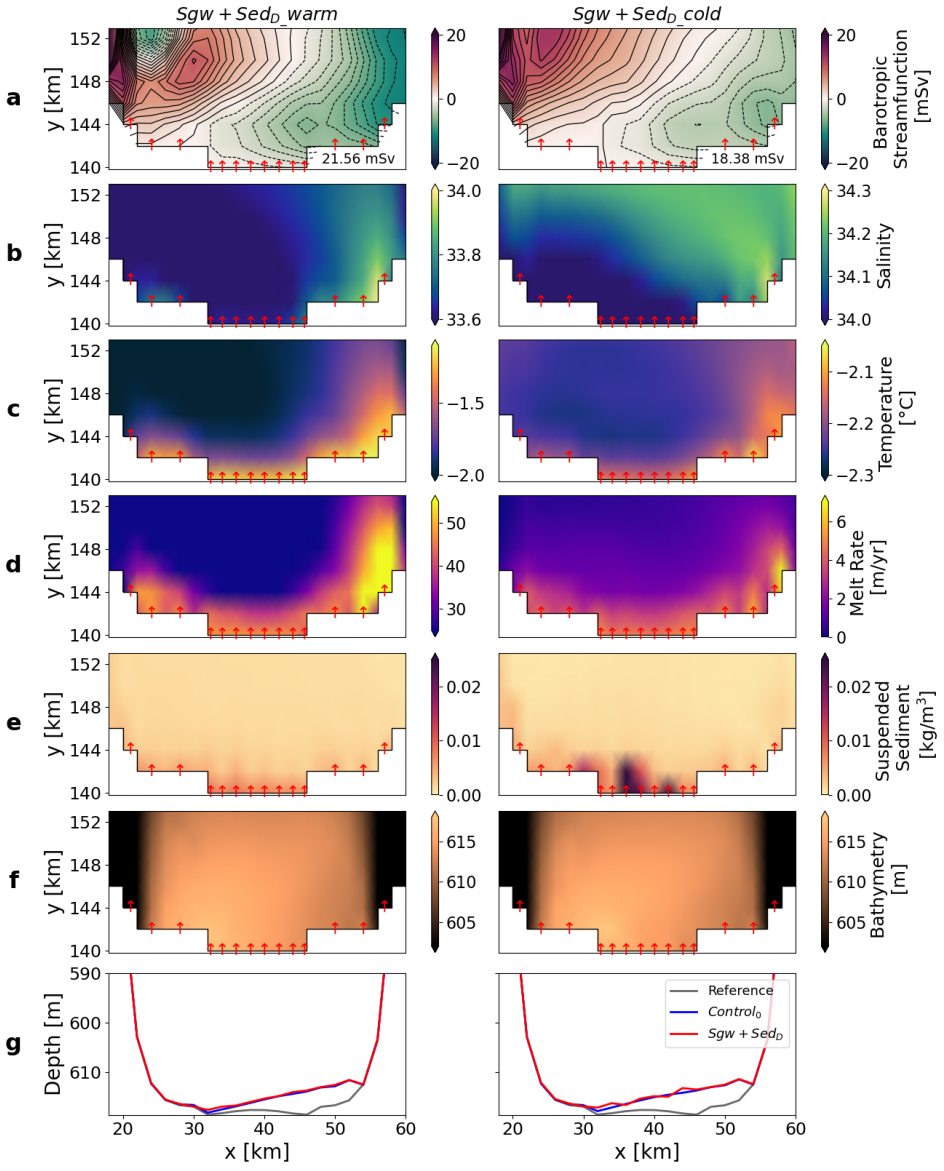

Figure 6. Warm and cold regimes absolute values from the simulations with distributed sediment-laden subglacial freshwaters (*Sgw+Sed$_D$_warm* and *Sgw+Sed$_D$_cold*, respectively). Injection sites range from x=20 to x=58 and are indicated by red arrows. Panels display barotropic streamfunction (a), salinity (b) and temperature (c) at the uppermost ocean layer, melt rates (d), total concentration of suspended sediment in the water column (e), bathymetry (f) and a vertical cross-section of the grounding line geometry (g). In panel (a), the maximum positive barotropic streamfunction value for each experiment is indicated on the corresponding panel. In panel (g), the grounding line, which is non-linear in plan view, is projected onto a straightened along-grounding line coordinate, with values interpolated onto a common axis for visualization purposes. Note the differing colour scales used for salinity, temperature and melt rate fields.

https://doi.org/10.5194/egusphere-2026-3435
Preprint. Discussion started: 25 June 2026

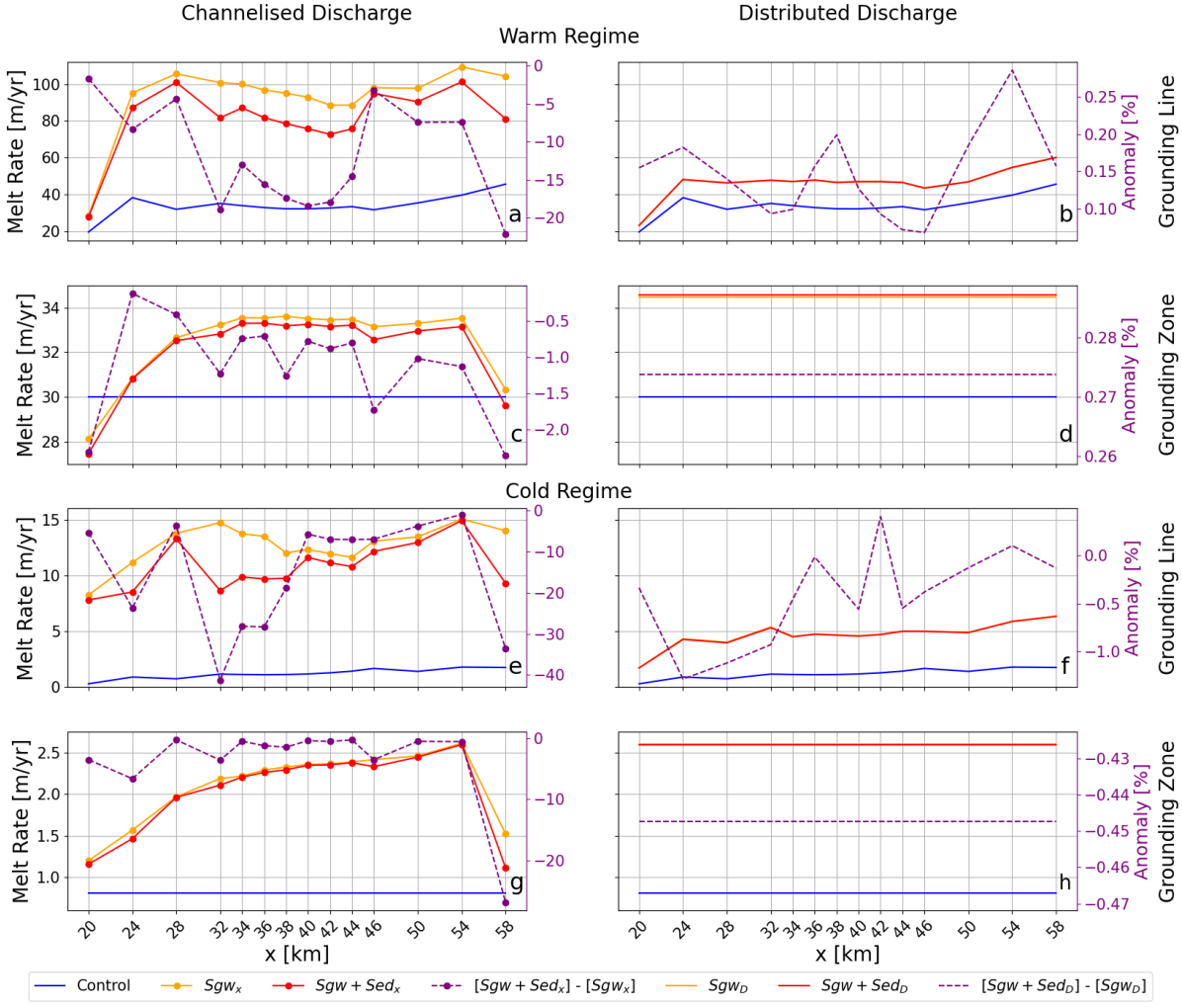

Figure 7. Melt rates and associated anomalies at the grounding line and grounding zone for the warm (top two rows) and cold (bottom two rows) regimes. The panels on the left (a, c, e, g) correspond to the channelised subglacial discharge experiments, and the panels on the right (b, d, f, h) represent distributed discharge experiments. Each subplot includes three experiments: $Control_0$ (blue), Sgw_x or Sgw_D (orange), and $Sgw{+}Sed_x$ or $Sgw{+}Sed_D$ (red). The purple dashed lines represent the differences between $Sgw{+}Sed_x$ and Sgw_x, or $Sgw{+}Sed_D$ and Sgw_D, highlighting the anomalies relative to the sediment-laden subglacial discharge. Lines with markers indicate point discharge locations, whereas continuous lines represent distributed discharge experiments. Absolute values of melt rates are plotted on the left y axes, while the percentages of anomalies are shown on the right y axes.

over the grounding zone. Comparisons between sediment-laden and freshwater-only simulations are used to distinguish the relative influence of subglacial sediment on basal melt variability.

https://doi.org/10.5194/egusphere-2026-3435
Preprint. Discussion started: 25 June 2026

Channelised discharges at the grounding line produce stronger melt responses, and highlight clear contrasts between warm and cold cavity regimes (Figure 7a,e). In the warm regime, *Control*$_0$*_warm* exhibits melt rates of approximately 20-45 m yr $^{-1}$. When freshwater-only forcing is added (*Sgw*$_x$*_warm*), melt rates increase by an average of 173 %, reaching around 90-110 m yr $^{-1}$ (Figure 7a). The inclusion of sediment (*Sgw+Sed*$_x$*_warm*) reduces melting to the range of 75-100 m yr $^{-1}$, producing negative anomalies of up to - 22 %, and with an average of - 13 % (relative to experiments that include only freshwater; *Sgw*$_x$*_warm*). In the cold regime, melt rates remain an order of magnitude lower overall, increasing from 1-2 m yr $^{-1}$ in the *Control*$_0$*_cold*, to 8-15 m yr $^{-1}$ in the *Sgw*$_x$*_cold*, representing an average increase of ∼955 % (Figure 7e). When subglacial sediment is included, melt rates decrease by an average of - 16 % to 7-15 m yr $^{-1}$. Although sediment-driven impacts are spatially variable, melt anomalies are generally reduced in central–eastern regions, where erosion-driven bathymetric lowering modifies the local circulation and limits melt enhancement.

For the grounding zone, averaged melt rates under channelised discharge preserve the same experiment response observed as at the grounding line, but with substantially lower magnitudes (Figure 7c,g). In the warm regime, while *Control*$_0$*_warm* has an average melt rate of ∼ 30 m yr $^{-1}$, the addition of subglacial freshwater results in an average increase of ∼9 % (*Sgw*$_x$*_warm*), with melt rates ranging between 27 and 34 m yr $^{-1}$, depending on channel location. When sediment is added (*Sgw+Sed*$_x$*_warm*), melt rate reductions are modest (- 2.5 % to - 0.1 %, relative to experiments that include only freshwater; *Sgw*$_x$*_warm*), and are generally more evident near cavity boundaries, where peripheral injections can have different impacts on grounding zone dynamics (Figures 3d and 7c). In the cold regime, melt rates remain an order of magnitude lower: *Control*$_0$*_cold* has an average melt rate of 0.8 m yr $^{-1}$, while *Sgw*$_x$*_cold* reaches 1.2-2.6 m yr $^{-1}$, increasing melt rates by ∼165 % on average (Figure 7g). The differences between freshwater-only and subglacial sediment channelised discharge experiments are generally small (0 to - 7 %), with an exception for the easternmost site, where the reduction approaches ∼ - 27 % (Figure 7g). Regardless of injection site location, the impact of subglacial sediment on melt rates is always negative under channelised discharge, either locally at the grounding line or averaged for the grounding zone (Figure 7c,g).

Distributed discharge produces substantially weaker melt responses at the grounding line than channelised configurations in both cavity regimes (Figure 7b,f). In the warm regime, the freshwater-only experiment (*Sgw*$_D$*_warm*) shows melt rates ranging between 20 and 60 m yr $^{-1}$, representing an increase of approximately 37 % relative to the control scenario *Control*$_0$*_warm*. The addition of subglacial sediment (*Sgw+Sed*$_D$*_cold*) results in minor positive anomalies (0.1 % to 0.27 %). In the cold regime, the *Sgw*$_D$*_cold* experiment produces melt rates that range from 2 to 6 m yr $^{-1}$: an increase of ∼ 287 % compared to the control. The addition of subglacial sediment has no consistent behaviour, with anomalies fluctuating between - 1.4 % and 0.4 % (Figure 7f). These results indicate that distributed sediment-laden discharge exerts only a minor influence on grounding line melt, with impacts varying spatially along the grounding line.

In the broader grounding zone, distributed discharge produces higher melt rates than channelised configurations in both cavity regimes (Figure 7d,h compared to 7c,g). Relative to their respective control experiments, freshwater-only forcing (*Sgw*$_D$*_warm* and *Sgw*$_D$*_cold*) increases melt rates by ∼ 4.5 m yr $^{-1}$ in the warm regime (Figure 7d) and by ∼2.1 m yr $^{-1}$ in the cold regime (Figure 7h), representing increases of ∼15 % and ∼223 %, respectively. The addition of subglacial sedi-

https://doi.org/10.5194/egusphere-2026-3435
Preprint. Discussion started: 25 June 2026

ment introduces only minor variations in grounding zone averaged melt, with anomalies of $\sim$0.29 % in the warm regime, and $\sim$ - 0.42 % in the cold regime, indicating a potentially negligible influence also at this spatial scale.

Overall, our results show that channelised discharges (*Sgw$_x$_warm*, *Sgw$_x$_cold*, *Sgw+Sed$_x$_warm*, *Sgw+Sed$_x$_cold*) generate stronger melt responses at the grounding line than distributed discharges (Figure 7a,b,e,f). However, the influence of distributed discharges (*Sgw$_D$_warm*, *Sgw$_D$_cold*, *Sgw+Sed$_D$_warm*, *Sgw+Sed$_D$_cold*) is higher over the grounding zone region (Figure 7c,d,g,h).

4 Discussion

Previous studies have consistently demonstrated that subglacial discharge enhances ice shelf basal melt near the grounding line. This fresh and buoyant outflow increases entrainment towards the ice base, driving stronger turbulent exchange to the ice-ocean interface (Le Brocq et al., 2013; Nakayama et al., 2021; Gwyther et al., 2023; Pelle et al., 2023; Vaňková et al., 2025; Papapetros et al., 2025). However, most of this framework emerged from investigations of warm ice shelf cavities, where relative strong background circulation reinforces buoyant-driven melt intensification. This warm-cavity focus has limited understanding of how contrasting background circulation states modulate the oceanic response to subglacial buoyancy forcing. To address this gap, we compared subglacial discharge responses under contrasting cavity regimes. Our results show that identical subglacial forcing can produce different dynamic responses depending on the background state, demonstrating the important role of cavity regime in modulating subglacial discharge impacts.

In warm cavities, buoyant subglacial discharge enhances the already energetic ambient field (Figures 2c and 3c), whereas in the cold regime, our results show that the same freshwater produces a larger impact on the weaker ambient circulation state (Figures 2c and 4c). Although absolute melt rate values remain higher in the warm cavity (Figures 2d and 4d), the respective percentage anomalies are larger in the cold regime (Figure 7), indicating that cold cavities may be dynamically more sensitive to subglacial discharge.

Importantly, the background regime further interacts with the location of subglacial discharge along the grounding line (Figures 2, 3 and 4). Our experiments show that the channelised discharge location determines whether the response remains channelised and boundary-confined, or expands to influence the cavity-wide circulation. Central grounding line injections tend to maximise lateral redistribution of heat and freshwater, whereas peripheral injections remain constrained by the cavity geometry. In contrast, when discharge is distributed along the grounding line, the subglacial water generates a weaker but spatially distributed buoyancy forcing that affects a broader region of the grounding zone. This partially aligns with the sensitivity to freshwater-only discharge configurations reported by Vaňková et al. (2025) for warm cavities, as both studies show enhanced grounding zone melt when freshwater input is spatially distributed. However, the west-to-east increase in melt identified in their channelised simulations was not reproduced here. This difference may result from our experimental design, with more discharge sites tested, as well as enhanced lateral and vertical mixing from tidal forcing (Gwyther et al., 2016). Additionally, the use of a different ocean model framework may also contribute to variations in circulation structure and buoyancy dynamics,

https://doi.org/10.5194/egusphere-2026-3435
Preprint. Discussion started: 25 June 2026

as reported by Yung et al. (2026), indicating that melt enhancement depends not only on the freshwater flux magnitude and the spatial configuration, but also on the relative background circulation, cavity forcing and regime.

A key outcome of our experiments is that subglacial discharge does not simply impose a localized melt perturbation at the grounding line. Instead, buoyancy forcing reorganizes the cavity circulation structure by modifying the location and strength of circulation cells. The resulting redistribution of heat and freshwater controls where melt enhancement occurs, and whether responses remain confined to the boundary regions or expand throughout the cavity. This impact on circulation is particularly pronounced in cold cavities, where weaker background circulation allows buoyancy forcing to exert proportionally larger dynamical influence over grounding zone circulation patterns.

Beyond the traditional division between warm and cold conditions, our results suggest a broader conceptual revision in the classification of ice shelves. Rather than a one-dimensional spectrum governed by temperature and melt rates, our findings support the existence of multiple dynamic grounding zone regimes that can produce comparable melt outcomes. Within this framework, a predominantly cold cavity can still exhibit high melt rates when subjected to strong subglacial discharge forcing, indicating that melt response is not uniquely tied to thermal conditions alone. This behaviour suggests that basal melting may emerge from a more complex interplay of physical processes, allowing for transitions between relatively quiescent and more dynamic states. Consequently, ice shelves may be better understood as complex systems operating within a multidimensional state space, where different combinations of conditions can lead to comparable melt signatures.

Beyond freshwater-driven effects, our results also highlight an additional layer of complexity introduced by sediment-laden discharge. While suspended sediment modifies the buoyancy flux density (Salcedo-Castro et al., 2013; Papapetros et al., 2025), its direct influence on melt rates and cavity circulation remains comparatively weak when sediment input is spatially distributed along the grounding line (Figures 3 and 4). In contrast to the distributed subglacial water experiments, where buoyancy outflows generate a spatially extensive melt response, adding distributed sediment discharge makes a negligible change to melt rates (maximum of - 1.4 % at the grounding line and $\sim$ - 0.42 % in the wider grounding zone; Figure 7). This is because the distributed sediment discharge results in a diffuse sediment concentration, limiting the development of strong and focused circulation reorganization. Instead, the dominant impact of sediment emerges through localised bathymetric feedbacks, consistent with Papapetros et al. (2025). In the warm cavity (Figure 3), strong background circulation suppresses sustained depositional thickening and minimises bathymetric feedbacks on melt rates. In contrast, the slower circulation in the cold cavity (Figure 4) facilitates local deposition of coarser grains and the formation of sand-rich beds with low critical shear stress (Figure 5), promoting episodic erosion and substantial seabed rearrangement. These bathymetric adjustments alter circulation pathways (Zhou and Hattermann, 2020) and modulate melt rates (Papapetros et al., 2025), reinforcing that sediment influence operates primarily through morphodynamic feedback.

Along with the cavity geometry, the contrasting sediment dynamics between regimes imply different pathways for grounding zone wedge (GZW) development (Batchelor and Dowdeswell, 2015; Horgan et al., 2013). The enhanced deposition in the cold regime provides favourable conditions for GZW formation; however, the predominance of sand-rich deposits may limit the long-term accretion of these features, as non-cohesive sediments are less stable due to its low critical erosion stress thresholds. In the warm cavity, by contrast, reduced sediment retention may slow the initial wedge formation, yet deposited material is

https://doi.org/10.5194/egusphere-2026-3435
Preprint. Discussion started: 25 June 2026

less frequently destabilised, potentially favouring more persistent morphological features once established. This emphasises the importance of sediment composition in controlling bathymetric feature stability (Li et al., 2022; Smith et al., 2019), as cohesive mud-rich deposits tend to resist erosion more effectively, whereas non-cohesive sand-rich deposits are more susceptible to remobilisation under comparatively weak flow perturbations. Furthermore, recurring seabed reworking could also inhibit the progressive build-up required for a stable and consolidated GZW. These results suggest that the cavity thermal regime may also play an important role not only in sediment depositional rates, but also in the structural integrity and longevity of grounding zone wedges, with potential implications for their effectiveness as stabilising pinning points.

The sediment loads prescribed in our simulations fall within the range of previously reported subglacial sediment concentrations, which span approximately 0.3 – 1 kg m^{-3} (Chu et al., 2009; Schild et al., 2017; Aitken et al., 2024). These estimates remain highly uncertain due to poorly constrained erosion rates and variability in subglacial drainage efficiency. Given the limited observational constraints, we adopt representative concentrations within this range to explore first-order sediment–circulation feedbacks, rather than to represent discharge periodicity or extreme scenarios. Variations in sediment flux are expected to influence buoyancy outflow and sediment entrainment (Delaney et al., 2019, 2025), and therefore affect the magnitude and spatial distribution of basal melt. Nevertheless, improved observational constraints on sediment discharge at grounding lines remain critical for quantifying their long-term impact.

Together, our results demonstrate that subglacial discharge exerts a fundamental control on grounding zone dynamics, whereby sediment-laden buoyant outflows reorganise circulation and melt patterns across the entire cavity rather than acting as a localised perturbation at the grounding line. The interaction between cavity regime and discharge location therefore determines whether the system response remains boundary-confined or expands into a cavity-scale reorganisation of thermohaline structure, circulation, and sediment redistribution. These findings suggest that models that include only ice-ocean interactions, while neglecting subglacial discharge and sediment transport processes, may underestimate the complexity of grounding zone evolution and its influence on spatial melt variability. More broadly, the processes identified here are likely to persist in realistic Antarctic settings, where complex bathymetry, multiple discharge outlets, tidal forcing, and temporal variability in freshwater input may modulate, but not remove, the underlying regime dependence.

In these simulations, the grounding line is fixed. In reality, sediment redistribution may modify bed morphology and grounding line stability, which would in turn feed back onto cavity geometry and circulation, potentially amplifying the regime-dependent behaviours identified here. Our experiments therefore provide a conservative estimate of sediment-laden subglacial discharge feedback processes that may be important for grounding zone evolution. Fully coupled simulations are required to quantify how these interactions evolve under sustained forcing and to assess their implications for long-term ice sheet stability.

5 Conclusions

In this study, we used idealised ice shelf-ocean simulations coupled with sediment processes to investigate how subglacial discharge location, configuration, and sediment load interact under contrasting warm and cold cavity regimes. By examining both

https://doi.org/10.5194/egusphere-2026-3435
Preprint. Discussion started: 25 June 2026

oceanographic and morphodynamic responses, we aim to better constrain how subglacial freshwater and sediment processes jointly influence basal melt, cavity circulation, and grounding zone dynamics.

Overall, our findings demonstrate that ocean cavity regimes have an important influence on the impact of subglacial discharge on ice shelf cavities and basal melting, with cold cavities exhibiting a substantially higher relative sensitivity to freshwater forcing than warm cavities (grounding line melt rate increases up to $\sim$955 % in the cold regime, and $\sim$173 % in the warm regime). This sensitivity is further modulated by discharge configuration, which determines whether buoyancy-driven impacts remain locally confined or distributed at the grounding zone. While sediment-laden discharge exerts a consistent grounding line melt-reducing effect under channelised conditions ($\sim$ 13% reduction in the warm regime and $\sim$ 16% in the cold regime), its influence is negligible when discharge is spatially distributed (< 1 %). Importantly, the dominant influence of sediment is through morphodynamic feedbacks (Papapetros et al., 2025), which reshape the seabed and alter circulation patterns, particularly in cold cavities, where weaker circulation promotes sediment accumulation, unstable depositional environments, and episodic erosion events.

While melting is fundamentally driven by the heat availability at the ice-ocean interface, our results demonstrate the importance of coupled interactions among cavity circulation, tides, subglacial discharge, and sediment-driven morphodynamic feedbacks. The delivery of ocean heat to the ice base is further modulated by complex interactions between cavity thermal state, discharge configuration, sediment transport, and bathymetric changes. The complexity of these interacting processes presents a significant challenge for basal melt parametrisations in large-scale ice-ocean models, highlighting the need for regional approaches that better capture regime-specific and spatially heterogeneous grounding zone processes to improve projections of ice shelf vulnerability and Antarctic Ice Sheet stability.

Code and data availability.

The ocean model source code (Galton-Fenzi, 2019), its outputs and processing scripts (Papapetros, 2026) are publicly available.

Appendix A

A1

Figure A1 shows that all simulations reached a quasi-steady state over a 20 years period, defined here as a dynamic equilibrium in which domain-averaged melt rates plateaued. Simulations including subglacial discharge reached quasi-steady conditions more rapidly, as the enhanced buoyancy flux strengthened overturning circulation within the cavity and promoted earlier stabilization of melt rates compared to simulations without subglacial input.

https://doi.org/10.5194/egusphere-2026-3435
Preprint. Discussion started: 25 June 2026

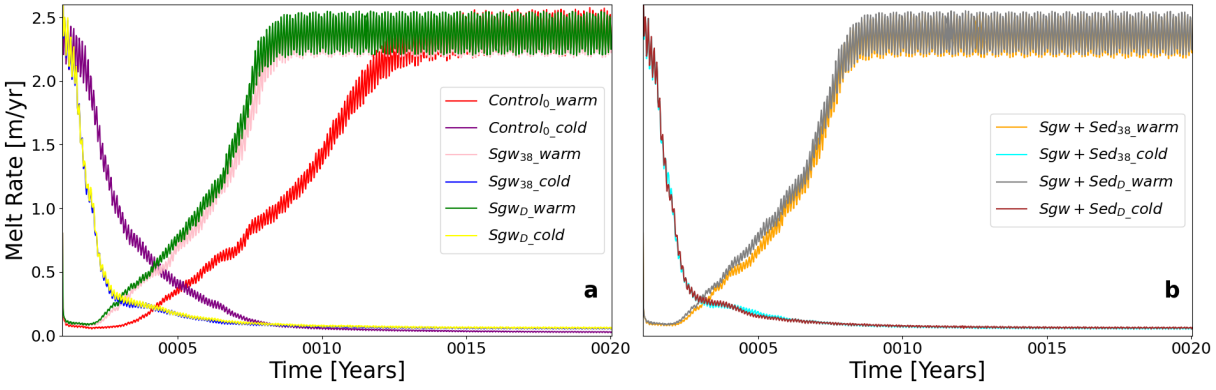

Figure A1. Domain-averaged melt rates spin-up over the 20-year simulation period. In panel (a), control experiments are shown as *Control*$_0$*_warm* (red) and *Control*$_0$*_cold* (purple), alongside representative simulations with centrally located subglacial discharge (x = 38 km) as *Sgw*$_{38}$*_warm* (pink) and *Sgw*$_{38}$*_cold* (blue), and distributed discharge as *Sgw*$_D$*_warm* (green) and *Sgw*$_D$*_cold* (yellow). Panel (b) shows the respective experiments that include sediment: *Sgw+Sed*$_{38}$*_warm* (orange), and *Sgw+Sed*$_{38}$*_cold* (light blue), *Sgw+Sed*$_D$*_warm* (grey) and *Sgw+Sed*$_D$*_cold* (brown).

A1

Figure A2 shows the bathymetry fields and for the controls (*Control*$_0$*_warm* and *Control*$_0$*_cold*; panel a), reference channelised discharges at location x = 38 km (*Sgw+Sed*$_{38}$*_warm* and *Sgw+Sed*$_{38}$*_cold*; panel c), and distributed discharges scenarios (*Sgw+Sed*$_D$*_warm* and *Sgw+Sed*$_D$*_cold*; panel e). In addition, the anomaly fields, in reference to the cold regime ([Cold]-[Warm]) are shown for each configuration to more clearly isolate the influence of cavity thermal regime on seafloor evolution (Figure A2b,d,f). Although the resulting bathymetric differences are relatively small in magnitude (approximately 0.15 - 0.17 cm), these modest variations help explain the contrasting suspended sediment distributions observed between cavity states, demonstrating that even minor morphodynamic adjustments can contribute to meaningful differences in sediment suspension and transport.

A2

To support the sediment classes differences described in our results, this section summarises the settling behaviour and bed evolution across cavity regimes. Panel (a) of Figure A3 compares grain size and settling velocity for each sediment classes (Mud1, Mud2, Sand1, and Sand2), illustrating the substantially faster settling of coarser particles relative to finer mud fractions. The settling velocities (w_s) were calculated using the formulation proposed by Ferguson and Church (2004), which describes the fall velocity of sediments in fluids across a wide range of grain sizes:

$$w_s = \frac{RgD^2}{C_1\nu + \sqrt{0.75 C_2 R g D^3}}$$

https://doi.org/10.5194/egusphere-2026-3435
Preprint. Discussion started: 25 June 2026

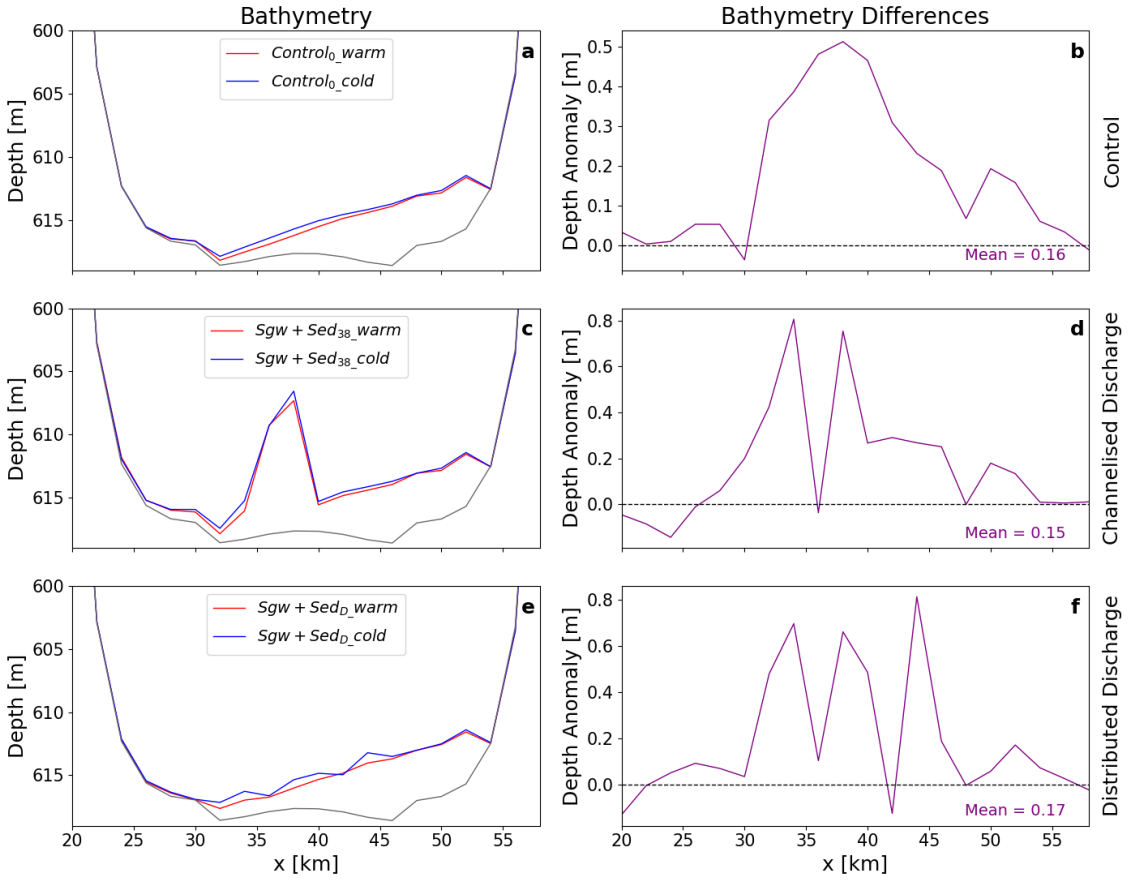

Figure A2. Bathymetric heights for control experiments (*Control$_0$_warm* and *Control$_0$_cold*; panel a), with channelised discharges at location x = 38 km (*Sgw+Sed$_{38}$_warm* and *Sgw+Sed$_{38}$_cold*; panel c), and with distributed discharges scenarios (*Sgw+Sed$_D$_warm* and *Sgw+Sed$_D$_cold*; panel e). The grey line in panels (a), (c), and (e) represent the reference bathymetry, with no sediment included. The respective anomalies reference between regimes (in reference to the cold scenario; [Cold]-[Warm]) are shown in panels (b), (d) and (f), emphasising the subtle seabed differences between contrasting thermal states. Dashed grey lines indicate zero, and the mean anomaly for each configuration is reported within the respective panels.

where R is the submerged specific density defined as $R = (\rho_s - \rho_f)/\rho_f$, with $\rho_s = 2650$ kg m^3 being the sediment grain density and ρ_f the fluid density estimated from temperature, salinity, and pressure using the TEOS-10 formulation (McDougall and Barker, 2011). The gravitational acceleration is g (9.81) m s^{-2}, and D is the grain diameter (m). The coefficients C_1 and C_2 account for viscous and turbulent drag effects, respectively, with values of $C_1 = 18$ and $C_2 = 1$.

Panel (b) of Figure A3 shows the bathymetric evolution over the 20-year simulation period for the reference experiments with channelised discharge at location x = 40 km (*Sgw+Sed$_{40}$_warm* and *Sgw+Sed$_{40}$_cold*). The analysis focuses on the grid cell immediately downstream of the discharge location, where the largest bathymetric increases are observed. The first three

https://doi.org/10.5194/egusphere-2026-3435
Preprint. Discussion started: 25 June 2026

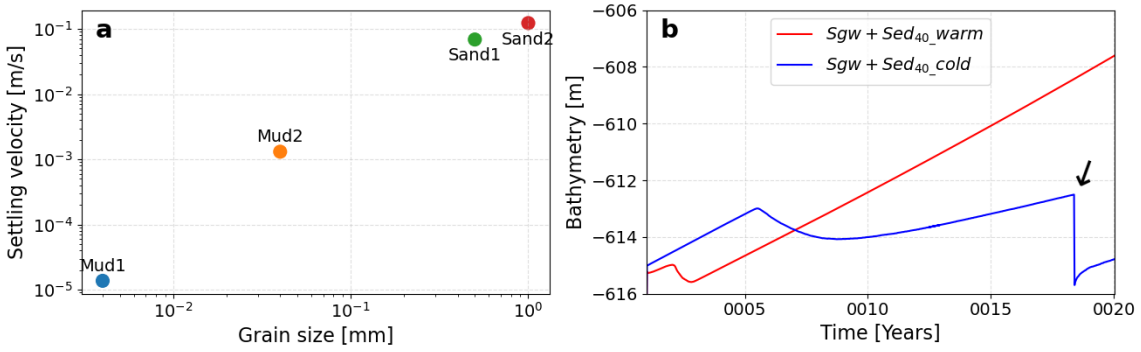

Figure A3. Sediment class properties and bathymetric evolution across cavity regimes. Panel (a) shows the relationship between grain size and settling velocity for the prescribed sediment classes (Mud1, Mud2, Sand1, and Sand2), highlighting the faster settling behaviour of coarser sediment fractions relative to finer mud particles. Panel (b) presents the bathymetric evolution throughout the 20-year experiment period for the reference channelised discharge simulations. The black arrow indicates the erosion event described in Section 3.2.

480 years are considered initial part of the model spin-up period, and are therefore excluded from the interpretation due to initial adjustment instabilities. Together, these results further demonstrate that background circulation strength directly influences grounding zone bathymetric evolution and sediment stability.

Author contributions.

Paola Papapetros (PP), Benjamin K. Galton-Fenzi (BGF), David E. Gwyther (DG), Fabio Boeira Dias (FBD), Sue Cook
485 (SC), and Chen Zhao (CZ) contributed to the conceptualization of this study. Methodology was developed by PP, BGF, DG, and FBD. Formal analysis and investigation were carried out by PP, BGF, DG, FBD, and SC. Funding acquisition was led by BGF and CZ.

Competing interests.

The authors declare no competing interests relevant to this study.

490 *Acknowledgements.* PP, CZ, SC, and BGF received grant funding from the Australian Government as part of the Antarctic Science Collaboration Initiative program (ASCI000002). PP, BGF, and FBD are supported by the Australian Research Council Special Research Initiative, Australian Centre for Excellence in Antarctic Science (Project SR200100008). CZ is the recipient of an Australian Research Council Discovery Early Career Researcher Award (Project DE240100267) funded by the Australian Government. DG was supported by Australian

https://doi.org/10.5194/egusphere-2026-3435
Preprint. Discussion started: 25 June 2026

Research Council Discovery Project Grant DP220102525. This research was undertaken on the National Computational Infrastructure (NCI
495 Australia), an NCRIS enabled capability supported by the Australian Government.

https://doi.org/10.5194/egusphere-2026-3435
Preprint. Discussion started: 25 June 2026

References

Aitken, A. R. A., Delaney, I., Pirot, G., and Werder, M. A.: Modelling subglacial fluvial sediment transport with a graph-based model, Graphical Subglacial Sediment Transport (GraphSSeT), The Cryosphere, 18, 4111–4136, https://doi.org/10.5194/tc-18-4111-2024, 2024.

Alley, R. B., Blankenship, D. D., Rooney, S. T., and Bentley, C. R.: Sedimentation beneath ice shelves — the view from Ice Stream B, Marine Geology, 85, 101–120, https://doi.org/10.1016/0025-3227(89)90053-4, 1989.

Alley, R. B., Anandakrishnan, S., Dupont, T. K., Parizek, B. R., and Pollard, D.: Effect of sedimentation on ice-sheet grounding-line stability, Science, 315, 1838–1841, https://doi.org/10.1126/science.1138396, 2007.

Anandakrishnan, S., Catania, G. A., Alley, R. B., and Horgan, H. J.: Discovery of Till Deposition at the Grounding Line of Whillans Ice Stream, Science, 315, 1835–1838, https://doi.org/10.1126/science.1138393, 2007.

Asay-Davis, X. S., Cornford, S. L., Durand, G., Galton-Fenzi, B. K., Gladstone, R. M., Gudmundsson, G. H., Hattermann, T., Holland, D. M., Holland, D., Holland, P. R., Martin, D. F., Mathiot, P., Pattyn, F., and Seroussi, H.: Experimental design for three interrelated marine ice sheet and ocean model intercomparison projects: MISMIP v. 3 (MISMIP+), ISOMIP v. 2 (ISOMIP+) and MISOMIP v. 1 (MISOMIP1), Geoscientific Model Development, 9, 2471–2497, https://doi.org/10.5194/gmd-9-2471-2016, 2016.

Batchelor, C. and Dowdeswell, J.: Ice-sheet grounding-zone wedges (GZWs) on high-latitude continental margins, Marine Geology, 363, 65–92, https://doi.org/https://doi.org/10.1016/j.margeo.2015.02.001, 2015.

Burton-Johnson, A., Dziadek, R., and Martin, C.: Review Article: Geothermal Heat Flow in Antarctica: Current and Future Directions, The Cryosphere, 14, 3391–3409, https://doi.org/10.5194/tc-14-3391-2020, 2020.

Chu, V. W., Smith, L. C., Rennermalm, A. K., Forster, R. R., Box, J. E., and Reeh, N.: Sediment plume response to surface melting and supraglacial lake drainages on the Greenland ice sheet, Journal of Glaciology, 55, 1072–1082, https://doi.org/10.3189/002214309790794904, 2009.

Delaney, I. and Adhikari, S.: Increased Subglacial Sediment Discharge in a Warming Climate: Consideration of Ice Dynamics, Glacial Erosion, and Fluvial Sediment Transport, Geophysical Research Letters, 47, e2019GL085 672, https://doi.org/10.1029/2019GL085672, 2020.

Delaney, I., Werder, M. A., and Farinotti, D.: A Numerical Model for Fluvial Transport of Subglacial Sediment, Journal of Geophysical Research: Earth Surface, 2019.

Delaney, I., Tedstone, A. J., Werder, M. A., and Farinotti, D.: Sediment Transport Capacity Response to Variations in Water Discharge in Pressurized Subglacial Channels, The Cryosphere, 19, 1–25, https://doi.org/10.5194/tc-19-1-2025, 2025.

Dinniman, M. S., Klinck, J. M., and Smith Jr., W. O.: Influence of sea ice cover and icebergs on circulation and water mass formation in a numerical circulation model of the Ross Sea, Antarctica, Journal of Geophysical Research: Oceans, 112, https://doi.org/https://doi.org/10.1029/2006JC004036, 2007.

Dow, C. F., Ross, N., Jeofry, H., et al.: Antarctic Basal Environment Shaped by High-Pressure Flow Through a Subglacial River System, Nature Geoscience, 15, 447–452, https://doi.org/10.1038/s41561-022-00994-z, 2022.

Dowdeswell, J. A. and Fugelli, E. M. G.: The Seismic Architecture and Geometry of Grounding-Zone Wedges Formed at the Marine Margins of Past Ice Sheets, GSA Bulletin, 124, 712–726, https://doi.org/10.1130/B30628.1, 2012.

Dowdeswell, J. A., Hogan, K. A., Arnold, N. S., Mugford, R. I., Wells, M., Hirst, J. P. P., and Decalf, C.: Sediment-rich meltwater plumes and ice-proximal fans at the margins of modern and ancient tidewater glaciers: Observations and modelling, Sedimentology, 62, 1665–1692, https://doi.org/https://doi.org/10.1111/sed.12198, 2015.

https://doi.org/10.5194/egusphere-2026-3435
Preprint. Discussion started: 25 June 2026

Dutrieux, P., Stewart, C., Jenkins, A., Nicholls, K. W., Corr, H. F. J., Rignot, E., and Steffen, K.: Basal Terraces on Melting Ice Shelves, Geophysical Research Letters, 41, 5506–5513, https://doi.org/10.1002/2014GL060618, 2014.

Edwards, T. L., Nowicki, S., Marzeion, B., et al.: Projected land ice contributions to twenty-first-century sea level rise, Nature, 593, 74–82, https://doi.org/10.1038/s41586-021-03302-y, 2021.

Ferguson, R. I. and Church, M.: A Simple Universal Equation for Grain Settling Velocity, Journal of Sedimentary Research, 74, 933–937, https://doi.org/10.1306/051204740933, 2004.

Fricker, H. A., Galton-Fenzi, B. K., Walker, C. C., Freer, B. I. D., Padman, L., and DeConto, R.: Antarctica in 2025: Drivers of Deep Uncertainty in Projected Ice Loss, Science, 387, 278–283, https://doi.org/10.1126/science.adu8315, 2025.

Galton-Fenzi, B.: Regional Ocean Modeling System (ROMS) source code [Software], https://doi.org/10.5281/zenodo.3526801, [Software], 2019.

Galton-Fenzi, B., Fricker, H. A., Bassis, J., Crawford, A., Gomez, N., and Schoof, C.: The Antarctic Ice Sheet and sea level: contemporary changes and future projections, in: Antarctica and Planet Earth, Taylor & Francis Group, 2025.

Galton-Fenzi, B. K., Hunter, J. R., Coleman, R., Marsland, S. J., and Warner, R. C.: Modeling the basal melting and marine ice accretion of the Amery Ice Shelf, Journal of Geophysical Research: Oceans, 117, https://doi.org/https://doi.org/10.1029/2012JC008214, 2012.

Gwyther, D. E., Cougnon, E. A., Galton-Fenzi, B. K., Roberts, J. L., Hunter, J. R., and Dinniman, M. S.: Modelling the response of ice shelf basal melting to different ocean cavity environmental regimes, Annals of Glaciology, 57, 131–141, https://doi.org/10.1017/aog.2016.31, 2016.

Gwyther, D. E., Dow, C. F., Jendersie, S., Gourmelen, N., and Galton-Fenzi, B. K.: Subglacial Freshwater Drainage Increases Simulated Basal Melt of the Totten Ice Shelf, Geophysical Research Letters, 50, e2023GL103 765, https://doi.org/https://doi.org/10.1029/2023GL103765, 2023.

Holland, D. M. and Jenkins, A.: Modeling thermodynamic ice–ocean interactions at the base of an ice shelf, Journal of Physical Oceanography, 29, 1787–1800, https://doi.org/10.1175/1520-0485(1999)029<1787:MTIOIA>2.0.CO;2, 1999.

Holland, P. R.: A model of tidally dominated ocean processes near ice shelf grounding lines, Journal of Geophysical Research: Oceans, 113, https://doi.org/https://doi.org/10.1029/2007JC004576, 2008.

Horgan, H. J., Christianson, K., Jacobel, R. W., Anandakrishnan, S., and Alley, R. B.: Sediment deposition at the modern grounding zone of Whillans Ice Stream, West Antarctica, Geophysical Research Letters, 40, 3934–3939, https://doi.org/https://doi.org/10.1002/grl.50712, 2013.

Horgan, H. J., Stewart, C., Stevens, C., et al.: A West Antarctic grounding-zone environment shaped by episodic water flow, Nature Geoscience, 18, 389–395, https://doi.org/10.1038/s41561-025-01687-3, 2025.

Huot, P.-V., Fichefet, T., Jourdain, N. C., Mathiot, P., Rousset, C., Kittel, C., and Fettweis, X.: Influence of ocean tides and ice shelves on ocean–ice interactions and dense shelf water formation in the D'Urville Sea, Antarctica, Ocean Modelling, 162, 101 794, https://doi.org/https://doi.org/10.1016/j.ocemod.2021.101794, 2021.

Jacobs, S. S., Hellmer, H. H., Doake, C. S. M., Jenkins, A., and Frolich, R. M.: Melting of ice shelves and the mass balance of Antarctica, Journal of Glaciology, 38, 375–387, https://doi.org/10.3189/S002214300000342X, 1992.

Jenkins, A.: Convection-Driven Melting Near the Grounding Lines of Ice Shelves and Tidewater Glaciers, Journal of Physical Oceanography, 41, 2279–2294, https://doi.org/10.1175/JPO-D-11-03.1, 2011.

https://doi.org/10.5194/egusphere-2026-3435
Preprint. Discussion started: 25 June 2026

Jeromson, M. R., Fujioka, T., Fink, D., Simon, K., Smith, J., Hillenbrand, C.-D., Kuhn, G., Post, A. L., Sánchez-Palacios, J. T., Blaxell, M., Enge, T. G., and White, D. A.: Circumpolar Deep Water upwelling is a primary source of 10Be in Antarctic continental shelf sediments, Global and Planetary Change, 236, 104 424, https://doi.org/https://doi.org/10.1016/j.gloplacha.2024.104424, 2024.

Large, W. G., McWilliams, J. C., and Doney, S. C.: Oceanic vertical mixing: A review and a model with a nonlocal boundary layer parameterization, Reviews of Geophysics, 32, 363–403, https://doi.org/https://doi.org/10.1029/94RG01872, 1994.

Le Brocq, Anne M., R. N., Griggs, J. A., Bingham, R. G., Corr, H. F. J., Ferraccioli, F., Jenkins, A., Jordan, T. A., Payne, A. J., Rippin, D. M., and Siegert, M. J.: Evidence from ice shelves for channelized meltwater flow beneath the Antarctic Ice Sheet, Nature Geoscience, 6, https://doi.org/10.1038/ngeo1977, 2013.

Lewis, E. L.: The "Ice Pump", a Mechanism for Ice-Shelf Melting, in: Glaciers, Ice Sheets, and Sea Level: Effect of a CO_2-Induced Climate Change, Department of Energy, United States, dOE/EV/60235-1, 1985.

Li, L., Aitken, A. R. A., Lindsay, M. D., et al.: Sedimentary Basins Reduce Stability of Antarctic Ice Streams Through Groundwater Feedbacks, Nature Geoscience, 15, 645–651, https://doi.org/10.1038/s41561-022-00978-z, 2022.

McDougall, T. J. and Barker, P. M.: Getting Started with TEOS-10 and the Gibbs Seawater (GSW) Oceanographic Toolbox, 28pp., SCOR/IAPSO WG127, 2011.

Nakayama, Y., Cai, C., and Seroussi, H.: Impact of Subglacial Freshwater Discharge on Pine Island Ice Shelf, Geophysical Research Letters, 48, e2021GL093 923, https://doi.org/https://doi.org/10.1029/2021GL093923, e2021GL093923 2021GL093923, 2021.

Overeem, I., Hudson, B., Syvitski, J., et al.: Substantial export of suspended sediment to the global oceans from glacial erosion in Greenland, Nature Geoscience, 10, 859–863, https://doi.org/10.1038/ngeo3046, 2017.

Padman, L., Siegfried, M. R., and Fricker, H. A.: Ocean Tide Influences on the Antarctic and Greenland Ice Sheets, Reviews of Geophysics, 56, 142–184, https://doi.org/https://doi.org/10.1002/2016RG000546, 2018.

Papapetros, P.: Model outputs and processing scripts [Dataset], https://doi.org/10.5281/zenodo.20652966, [Dataset], 2026.

Papapetros, P., Galton-Fenzi, B. K., Gwyther, D. E., Boeira Dias, F., and Zhao, C.: Effects of Sediment-Laden Subglacial Discharge on Ice Shelf Basal Melting and Seabed Evolution, Journal of Geophysical Research: Oceans, 130, e2025JC023 422, https://doi.org/10.1029/2025JC023422, 2025.

Parizek, B. R.: Grounding Zones: The "Inland" Dynamic Interface Between Seawater, Outlet Glaciers, Subglacial Meltwater Routing, and Ice-Shelf Processes, Geophysical Research Letters, 51, e2024GL110 427, https://doi.org/10.1029/2024GL110427, 2024.

Parizek, B. R., Christianson, K., Anandakrishnan, S., Alley, R. B., Walker, R. T., Edwards, R. A., Wolfe, D. S., Bertini, G. T., Rinehart, S. K., Bindschadler, R. A., and Nowicki, S. M. J.: Dynamic (in)stability of Thwaites Glacier, West Antarctica, Journal of Geophysical Research: Earth Surface, 118, 638–655, https://doi.org/https://doi.org/10.1002/jgrf.20044, 2013.

Pelle, T., Greenbaum, J. S., Dow, C. F., Jenkins, A., and Morlighem, M.: Subglacial discharge accelerates future retreat of Denman and Scott Glaciers, East Antarctica, Science Advances, 9, eadi9014, https://doi.org/10.1126/sciadv.adi9014, 2023.

Post, A., Galton-Fenzi, B., Riddle, M., Herraiz-Borreguero, L., O'Brien, P., Hemer, M., McMinn, A., Rasch, D., and Craven, M.: Modern sedimentation, circulation and life beneath the Amery Ice Shelf, East Antarctica, Continental Shelf Research, 74, 77–87, https://doi.org/https://doi.org/10.1016/j.csr.2013.10.010, 2014.

Pritchard, H., Ligtenberg, S., Fricker, H., et al.: Antarctic ice-sheet loss driven by basal melting of ice shelves, Nature, 484, 502–505, https://doi.org/10.1038/nature10968, 2012.

Reese, R., Gudmundsson, G. H., Levermann, A., and Winkelmann, R.: The Far Reach of Ice-Shelf Thinning in Antarctica, Nature Climate Change, 8, 53–57, https://doi.org/10.1038/s41558-017-0020-x, 2018.

https://doi.org/10.5194/egusphere-2026-3435
Preprint. Discussion started: 25 June 2026

Richter, O., Gwyther, D. E., Galton-Fenzi, B. K., and Naughten, K. A.: The Whole Antarctic Ocean Model (WAOM v1.0): development and evaluation, Geoscientific Model Development, 15, 617–647, https://doi.org/10.5194/gmd-15-617-2022, 2022a.

Richter, O., Gwyther, D. E., King, M. A., and Galton-Fenzi, B. K.: The impact of tides on Antarctic ice shelf melting, The Cryosphere, 16, 1409–1429, https://doi.org/10.5194/tc-16-1409-2022, 2022b.

Rosevear, M. G., Gayen, B., Vreugdenhil, C. A., and Galton-Fenzi, B. K.: How Does the Ocean Melt Antarctic Ice Shelves?, Annual Review of Marine Science, 17, 325–353, https://doi.org/10.1146/annurev-marine-040323-074354, 2025.

Salcedo-Castro, J., Bourgault, D., Bentley, S. J., and deYoung, B.: Non-hydrostatic modeling of cohesive sediment transport associated with a subglacial buoyant jet in glacial fjords: A process-oriented approach, Ocean Modelling, 63, 30–39, https://doi.org/https://doi.org/10.1016/j.ocemod.2012.12.005, 2013.

Schild, K. M., Hawley, R. L., Chipman, J. W., and Benn, D. I.: Quantifying suspended sediment concentration in subglacial sediment plumes discharging from two Svalbard tidewater glaciers using Landsat-8 and in situ measurements, International Journal of Remote Sensing, 38, 6865–6881, https://doi.org/10.1080/01431161.2017.1365388, 2017.

Schoof, C.: Ice sheet grounding line dynamics: Steady states, stability, and hysteresis, Journal of Geophysical Research: Earth Surface, 112, https://doi.org/https://doi.org/10.1029/2006JF000664, 2007.

Seroussi, H., Pelle, T., Lipscomb, W. H., Abe-Ouchi, A., Albrecht, T., Alvarez-Solas, J., Asay-Davis, X., Barre, J.-B., Berends, C. J., Bernales, J., Blasco, J., Caillet, J., Chandler, D. M., Coulon, V., Cullather, R., Dumas, C., Galton-Fenzi, B. K., Garbe, J., Gillet-Chaulet, F., Gladstone, R., Goelzer, H., Golledge, N., Greve, R., Gudmundsson, G. H., Han, H. K., Hillebrand, T. R., Hoffman, M. J., Huybrechts, P., Jourdain, N. C., Klose, A. K., Langebroek, P. M., Leguy, G. R., Lowry, D. P., Mathiot, P., Montoya, M., Morlighem, M., Nowicki, S., Pattyn, F., Payne, A. J., Quiquet, A., Reese, R., Robinson, A., Saraste, L., Simon, E. G., Sun, S., Twarog, J. P., Trusel, L. D., Urruty, B., Van Breedam, J., van de Wal, R. S. W., Wang, Y., Zhao, C., and Zwinger, T.: Evolution of the Antarctic Ice Sheet Over the Next Three Centuries From an ISMIP6 Model Ensemble, Earth's Future, 12, e2024EF004 561, https://doi.org/https://doi.org/10.1029/2024EF004561, e2024EF004561 2024EF004561, 2024.

Shchepetkin, A. F. and McWilliams, J. C.: The regional oceanic modeling system (ROMS): a split-explicit, free-surface, topography-following-coordinate oceanic model, Ocean Modelling, 9, 347–404, https://doi.org/https://doi.org/10.1016/j.ocemod.2004.08.002, 2005.

Sherwood, C. R., Aretxabaleta, A. L., Harris, C. K., Rinehimer, J. P., Verney, R., and Ferré, B.: Cohesive and mixed sediment in the Regional Ocean Modeling System (ROMS v3.6) implemented in the Coupled Ocean–Atmosphere–Wave–Sediment Transport Modeling System (COAWST r1234), Geoscientific Model Development, 11, 1849–1871, https://doi.org/10.5194/gmd-11-1849-2018, 2018.

Silvano, A., Rintoul, S. R., and Herraiz-Borreguero, L.: Ocean-Ice Shelf Interaction in East Antarctica, Oceanography, 29, 130–143, https://doi.org/10.5670/oceanog.2016.105, 2016.

Smith, B., Fricker, H. A., Gardner, A. S., Medley, B., Nilsson, J., Paolo, F. S., Holschuh, N., Adusumilli, S., Brunt, K., Csatho, B., Harbeck, K., Markus, T., Neumann, T., Siegfried, M. R., and Zwally, H. J.: Pervasive ice sheet mass loss reflects competing ocean and atmosphere processes, Science, 368, 1239–1242, https://doi.org/10.1126/science.aaz5845, 2020.

Smith, J., Graham, A., Post, A., et al.: The marine geological imprint of Antarctic ice shelves, Nature Communications, 10, 5635, https://doi.org/10.1038/s41467-019-13496-5, 2019.

Sutherland, B. R., Rosevear, M. G., and Cenedese, C.: Laboratory experiments modeling the transport and deposition of sediments by glacial plumes rising under an ice shelf, Phys. Rev. Fluids, 5, 013 802, https://doi.org/10.1103/PhysRevFluids.5.013802, 2020.

Vaňková, I., Asay-Davis, X., Branecky Begeman, C., Comeau, D., Hager, A., Hoffman, M., Price, S. F., and Wolfe, J.: Subglacial discharge effects on basal melting of a rotating, idealized ice shelf, The Cryosphere, 19, 507–523, https://doi.org/10.5194/tc-19-507-2025, 2025.

https://doi.org/10.5194/egusphere-2026-3435
Preprint. Discussion started: 25 June 2026

Wang, H., Chen, Z., Wang, K., Liu, H., Tang, Z., and Huang, Y.: Characteristics of heavy minerals and grain size of surface sediments on the continental shelf of Prydz Bay: implications for sediment provenance, Antarctic Science, 28, 103–114, https://doi.org/10.1017/S0954102015000498, 2016.

Wright, L. D. and Thom, B. G.: Coastal Morphodynamics and Climate Change: A Review of Recent Advances, Journal of Marine Science and Engineering, 11, https://doi.org/10.3390/jmse11101997, 2023.

Xia, Y., Gwyther, D. E., Galton-Fenzi, B., Cougnon, E. A., Fraser, A. D., and Moore, J. C.: Eddy and tidal driven basal melting of the Totten and Moscow University ice shelves, Frontiers in Marine Science, 10, https://doi.org/10.3389/fmars.2023.1159353, 2023.

Yung, C. K., Rosevear, M. G., Morrison, A. K., Hogg, A. M., and Nakayama, Y.: Stratified suppression of turbulence in an ice shelf basal melt parameterisation, The Cryosphere, 19, 5827–5861, https://doi.org/10.5194/tc-19-5827-2025, 2025.

Yung, C. K., Asay-Davis, X. S., Adcroft, A., Bull, C. Y. S., De Rydt, J., Dinniman, M. S., Galton-Fenzi, B. K., Goldberg, D., Gwyther, D. E., Hallberg, R., Harrison, M., Hattermann, T., Holland, D. M., Holland, D., Holland, P. R., Jordan, J. R., Jourdain, N. C., Kusahara, K., Marques, G., Mathiot, P., Menemenlis, D., Morrison, A. K., Nakayama, Y., Sergienko, O., Smith, R. S., Stern, A., Timmermann, R., and Zhou, Q.: Results of the second Ice Shelf–Ocean Model Intercomparison Project (ISOMIP+), The Cryosphere, 20, 2053–2088, https://doi.org/10.5194/tc-20-2053-2026, 2026.

Zhou, Q. and Hattermann, T.: Modeling ice shelf cavities in the unstructured-grid, Finite Volume Community Ocean Model: Implementation and effects of resolving small-scale topography, Ocean Modelling, 146, 101 536, https://doi.org/https://doi.org/10.1016/j.ocemod.2019.101536, 2020.